Electron Cooling with Graphene-Insulator-Superconductor Tunnel Junctions for Applications in Fast Bolometry

Francesco Vischi,[1,2,*] Matteo Carrega,[1] Alessandro Braggio,[1] Federico Paolucci,[1,3] Federica Bianco,[1,2] Stefano Roddaro,[1,2] and Francesco Giazotto[1]

[1] *NEST, Istituto Nanoscienze-CNR and Scuola Normale Superiore, Piazza S. Silvestro 3, I-56127 Pisa, Italy*
[2] *Dipartimento di Fisica "E. Fermi", Università di Pisa, Largo Bruno Pontecorvo 3, I-56127 Pisa, Italy*
[3] *INFN Sezione di Pisa, Largo Bruno Pontecorvo 3, I-56127 Pisa, Italy*

(Received 26 June 2019; revised manuscript received 21 October 2019; accepted 25 March 2020; published 4 May 2020)

Electronic cooling in hybrid normal-metal–insulator–superconductor junctions is a promising technology for the manipulation of thermal loads in solid-state nanosystems. One of the main bottlenecks for efficient electronic cooling is the electron-phonon coupling, as it represents a thermal leakage channel to the phonon bath. Graphene is a two-dimensional material that exhibits a weaker electron-phonon coupling compared to standard metals. For this reason, we study the electron cooling in graphene-based systems consisting of a graphene sheet contacted by two insulator-superconductor junctions. We show that, by properly biasing the graphene, its electronic temperature can reach base values lower than those achieved in similar systems based on metallic ultrathin films. Moreover, the lower electron-phonon coupling is mirrored in a lower heat power pumped into the superconducting leads, thus avoiding their overheating and preserving the cooling mechanisms. Finally, we analyze the possible application of cooled graphene as a bolometric radiation sensor. We study its main figures of merit, i.e., responsivity, noise equivalent power, and response time. In particular, we show that the built-in electron refrigeration allows reaching a responsivity of the order of 50 nA/pW and a noise equivalent power of order of 10^{-18} W $Hz^{-1/2}$ while the response speed is about 10 ns corresponding to a thermal bandwidth in the order of 20 MHz.

DOI: 10.1103/PhysRevApplied.13.054006

I. INTRODUCTION

Low-temperature physics at the micro and nanoscale has found many practical applications in ultrafast electronics for computing [1–8], low-noise high-sensitivity magnetometers [9–12], radiation sensors, and detectors [13–22]. Hence, finding alternative and efficient cooling schemes is of primary importance [23,24]. Typically, ultralow-temperature cryogenics is accomplished mainly by exploiting He^3/He^4 systems consisting of expensive and bulky machines, with unavoidable issues for space or portable applications. For this reason, important efforts are spent in the field of solid-state cooling to realize microrefrigerators that can be efficient and scalable to an industrial standard. Many different systems have been proposed, based for example on chiral Hall channels [25–28], adiabatic magnetization [29,30], piezoelectric elements [31], quantum dots [32–34], single ions [35], and engines based on superconducting circuits [36–40].

A cornerstone in this field is the electron refrigeration in voltage-biased normal-metal–insulator–superconductor (N-I-S) tunnel junctions [41,42]. In such a system, the gap of the superconductor acts as an energy filter for the N metal electrons: under an appropriate voltage bias, only the most energetic electrons, i.e., the hottest ones, are able to tunnel into the superconductor, resulting in a decrease of temperature in the N metal [23,24,41,42]. The performance of this system is adversely affected by two main phenomena. One consists of an intrinsic thermal leakage owing to the electron-phonon (e-ph) coupling [23]. The phonons of the metal can be considered as a thermal bath, the temperature of which is set by the substrate temperature. Phonons interact with electrons over the metal volume, consequently supplying heat. Secondly, the heat extracted from the N metal warms up the superconducting leads, with the consequent decrease of the superconducting gap and deterioration of the energy filtering over the electrons [43–45].

In this paper, we study the graphene refrigeration based on two graphene-insulator-superconductor (G-I-S) tunnel junctions forming a S-I-G-I-S system. Graphene has several interesting properties compared to metals, for example, a density of states dependent on carrier concentration [46], and a weaker and gate tunable electron-phonon coupling [47,48]. The weak electron-phonon coupling arises from the graphene dimensionality [49], as tested in other

*francesco.vischi@df.unipi.it

low-dimension materials [50,51]. As a consequence, for given cooling power, a *S-I-G-I-S* can reach lower temperatures compared to a *S-I-N-I-S* system. Moreover, the lower heat current pumped into the leads decreases their adverse heating, making electron cooling more accessible for concrete applications.

A natural application of electron cooling in *S-I-G-I-S* systems concerns the detection of electromagnetic radiation via bolometric effect. It is known that *S-I-N-I-S* systems can be used as bolometers, where the built-in refrigeration enhances the responsivity and decreases the noise equivalent power (NEP) [52–57]. A *S-I-G-I-S*-based bolometer inherits the advantages of built-in refrigeration from a *S-I-N-I-S* system, combining them with graphene optoelectronic properties [13], such as wide energy absorption spectrum, ultrafast carrier dynamics [58–62], and tunable optical properties via electrostatic doping [63,64]. In particular, the lower operating temperature and the weaker electron-phonon coupling allow further decreasing the NEP, while the graphene low heat capacity allows a faster response time compared to a *S-I-N-I-S* bolometer.

From the industrial point of view, *S-I-G-I-S* systems may also have high potentiality in wafer-scale integration thanks to the high quality currently reached in large-area graphene production [65]. Moreover, the tunnel junction can be realized with hexagonal boron nitride (*h*-BN), which is an insulating material extremely suitable to be combined with graphene due to the crystal similarities. Tunnel barriers based on *h*-BN represent a valuable alternative to standard metal oxide insulators, simplifying the fabrication into standard steps [66].

The paper is organized as follows. Section II introduces the device model, the *G-I-S* tunneling, and the thermal model. Section III studies the graphene base temperature in a biased *S-I-G-I-S*, also giving a comparison with a standard *S-I-N-I-S* system. Section IV investigates the system response to perturbations and the related dynamical response time. In Sec. V, we study the bolometric properties by focusing on the responsivity and the NEP. Section VI discusses the impact of the junction quality on the studied properties and yields a quantitative threshold for experiments. Section VII compares our findings with similar bolometric architectures. Finally, Sec. VIII summarizes our main findings.

II. MODEL

We consider the system sketched in Fig. 1. It consists of a graphene sheet contacted by two superconducting leads through tunnel junctions of resistance R_t each. Superconductors are assumed to be made of aluminum with superconducting gap $\Delta_0 = 200\ \mu$eV and critical temperature $T_c \sim 1.3$ K. The graphene can be deposited directly on SiO_2 or *h*-BN. The graphene sheet has a rectangular area, with geometrical dimensions $A = W \times L$. The two

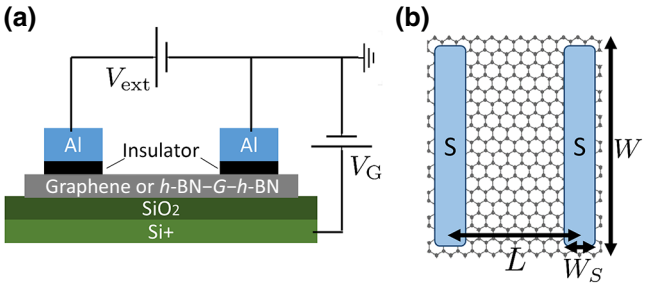

FIG. 1. Sketch of the device. (a) A graphene sheet or *h*-BN-encapsulated graphene is in contact with two aluminum leads through a tunnel junction with resistance R_t. In the case of *h*-BN-encapsulated graphene, the insulators can be provided by the *h*-BN layer itself. A voltage bias V_{ext} is applied to the two leads. A backgate, biased with a voltage V_G, allows tuning carrier density on the graphene sheet. (b) View from the top. The graphene geometrical dimensions are W and L, with resulting sheet resistance R_G and area A. The superconducting leads are wide W_S.

leads, with dimensions $W \times W_S$, are placed at distance L [see Fig. 1(b)] and connected to a voltage generator V_{ext}. The electric current I is determined by R_t and the graphene sheet resistance $R_G = L\rho/W$, where the sheet resistivity $\rho = 1/en\mu$ depends on the carrier density n and the electron mobility μ, with e being the modulus of the electron charge. The graphene is gated with a backgate placed under the substrate and connected to an external generator V_G.

The proposed setup has many geometrical and fabrication parameters. As a consequence, we fix some of them to reasonable experimental values. By choosing proper geometrical dimensions for the graphene sheet, we consider a negligible sheet resistance compared to the tunnel resistance ($R_G \ll R_t$). This assumption allows neglecting the voltage partition between the junctions and the sheet. So, the Joule heating of graphene is negligible. To this aim, we set the aspect ratio to $L = W/5$, corresponding to $R_G \approx 250\ \Omega$ for graphene with $\mu \approx 5000\ \mathrm{cm}^2/\mathrm{Vs}$ and residual carrier density $n_0 \approx 1 \times 10^{12}\ \mathrm{cm}^{-2}$, typical for graphene on SiO_2 [67–69]. A similar value of resistance can be considered for an encapsulated graphene in a *h*-BN–*G*–*h*-BN heterostructure, where mobilities are commonly over $\mu \approx 50\,000\ \mathrm{cm}^2/\mathrm{Vs}$ but the residual charge densities are lower than $n_0 \approx 1 \times 10^{11}\ \mathrm{cm}^{-2}$ [70–73]. An advantage of the encapsulated graphene is that the top layer of ultrathin *h*-BN can be exploited as a high-quality tunnel junction [66].

We consider a large graphene area $A = 100\ \mu\mathrm{m}^2$. Large area samples are preferred for bolometric applications since they keep the device in linear response regime and extend the dynamical range of the detector [14,74]. Moreover, a greater area reduces the temperature fluctuations, since the thermal inertia due to the heat capacity scales with the area.

TABLE I. Parameters used in the numerical calculations for the device under investigation.

Graphene dimensions	$L \times W = 4.5\ \mu\text{m} \times 22\ \mu\text{m}$
Graphene area	$A = 100\ \mu\text{m}^2$
Residual electron density	$n = 10^{12}\ \text{cm}^{-2}$
Tunnel resistance	$R_t = 10\ \text{k}\Omega$
Sheet resistance	$R_G = 250\ \Omega$
Electron-phonon coupling	$\Sigma_D = 23\ \text{mWm}^{-2}\,\text{K}^{-3}$ (dirty case)
	$\Sigma_C = 24\ \text{mWm}^{-2}\,\text{K}^{-4}$ (clean case)
Heat capacity at 0.5 K	$C = 34\ \text{zJK}^{-1} \approx 2.4 \times 10^3 k_B$

Finally, we fix the tunnel resistance as $R_t = 10\ \text{k}\Omega$. This value is compatible with tunnel junction made of two-layer h-BN [47,66] and makes the assumption $R_t \gg R_G$ valid. We also observe that the tunnel barriers suppress the superconducting proximity effect in graphene.

Table I is a summary of the parameters adopted in the numerical simulations. Some of them are introduced in the following.

A. *G-I-S* tunneling and cooling

Here, we introduce the main equations and discuss the electron tunneling through a *G-I-S* junction. The tunneling rate is proportional to the density of states (DOS) of graphene and superconductor [75]. The graphene DOS ν_G reads [46]

$$\nu_G = \rho_{G0}\rho_G(\epsilon), \quad \rho_G(\epsilon) = \frac{\epsilon}{E_F}, \tag{1}$$

where ϵ is the energy, ρ_{G0} is the DOS at the Fermi level, $\rho_G(\epsilon)$ is the normalized graphene DOS, and E_F is the Fermi energy. The DOS at the Fermi level is related to the carrier density by $\rho_{G0} = 2E_F/\pi\hbar^2 v_F^2$ and $E_F = \hbar v_F\sqrt{\pi n}$ where $v_F \approx 10^6$ m/s is the Fermi velocity [46] and $\hbar \approx 6.6 \times 10^{-16}$ eV s is the reduced Planck constant.

The superconductor DOS is

$$\nu_S = \rho_{S0}\rho_S(\epsilon), \tag{2}$$

$$\rho_S(\epsilon) = \left|\text{Re}\frac{(\epsilon + i\Gamma_D)}{\sqrt{(\epsilon + i\Gamma_D)^2 - \Delta^2(T)}}\right|, \tag{3}$$

where ϵ is the energy, ρ_{S0} is the DOS at Fermi level of the normal state aluminum, $\rho_S(\epsilon)$ is the superconductor normalized DOS, $\Delta(T)$ is the temperature-dependent superconductivity gap of the Bardeen-Cooper-Schrieffer (BCS) theory and Γ_D is the Dynes parameter that phenomenologically takes into account the subgap tunneling and the smearing of the superconducting peaks, which are also related to the quality of the junction. In this paper, we fix $\Gamma_D = 10^{-4}\Delta_0$, for simplicity. In Sec. VI, we show the dependence of the results on higher values of Γ_D.

The charge current in a *G-I-S* tunnel junction can be expressed as [47,75]

$$I(V, T_G, T_S) = \frac{1}{eR_t}\int_{-\infty}^{\infty} d\epsilon\ \{\rho_G(\epsilon - eV - E_F) \times \rho_S(\epsilon)[f(\epsilon - eV, T_G) - f(\epsilon, T_S)]\}, \tag{4}$$

where V is the voltage drop across the tunnel junction, T_G and T_S are the graphene and superconductor electronic temperatures, respectively. Finally, $f(\epsilon, T)$ is the Fermi distribution. In the following we assume that $V = V_{\text{ext}}/2$.

Similarly, the heat current from G to S is

$$P_{G\text{-}I\text{-}S}(V, T_G, T_S) = \frac{1}{e^2R_t}\int_{-\infty}^{\infty} d\epsilon\ \{(\epsilon - eV) \times \rho_G(\epsilon - eV - E_F)\rho_S(\epsilon)[f(\epsilon - eV, T_G) - f(\epsilon, T_S)]\}. \tag{5}$$

We set the sign convention such that $P_{G\text{-}I\text{-}S} > 0$ means that the heat is extracted from graphene towards superconductors. It is important to note that when the graphene Fermi energy E_F is much greater than the superconducting gap Δ_0, the graphene DOS dependence on energy can be disregarded in the tunneling integrals, i.e., $\rho_G(\epsilon - eV - E_F) \approx 1$. Indeed, for $eV, k_BT_S, k_BT_G \lessapprox \Delta_0$, the distribution $[f(\epsilon - eV, T_G) - f(\epsilon, T_S)]$ defines an energy bandwidth of a few Δ_0 around the Fermi level. In this energy window, the graphene DOS has a variation of the order of Δ_0/E_F that can be hence neglected when $E_F \gg \Delta_0$. This condition, in general, holds experimentally, as indicated by the presence of a residual charge density n_0 [72]. The lowest values of residual charge density can be obtained in high-quality h-BN–G–h-BN heterostructures and unlikely goes below $n_0 \approx 5 \times 10^{10}\ \text{cm}^{-2}$ [76]; this value corresponds to the lowest value of Fermi energy $E_F = \hbar v_F\sqrt{\pi n_0} \approx 26$ meV, that is at least 100 times the value of $\Delta_0 = 0.2$ meV, confirming $\Delta_0 \ll E_F$. We remark that the BCS theory provides that $\Delta(T) < \Delta_0$, implying that $E_F \gg \Delta_0 > \Delta(T)$, i.e., ensuring that the superconducting gap is lower than the Fermi energy at every temperature.

Therefore, tunneling integrals in Eqs. (4) and (5) take the standard functional form of the N-I-S tunneling expressions [23,24,77,78]. We point out that this approximation does not completely drop out the dependence of the tunnel integrals on the Fermi level and carrier density. It is indeed still contained in R_t. We discuss this point better at the end of this subsection.

Figure 2(a) displays the behavior of $P_{G\text{-}I\text{-}S}$ vs V and T_G is equal to the bath temperature T_B. In the regions where $P_{G\text{-}I\text{-}S} > 0$, the heat is extracted from graphene, implying electron cooling. It corresponds to the yellow-green area delimited by the white curve ($P_{G\text{-}I\text{-}S} = 0$). The

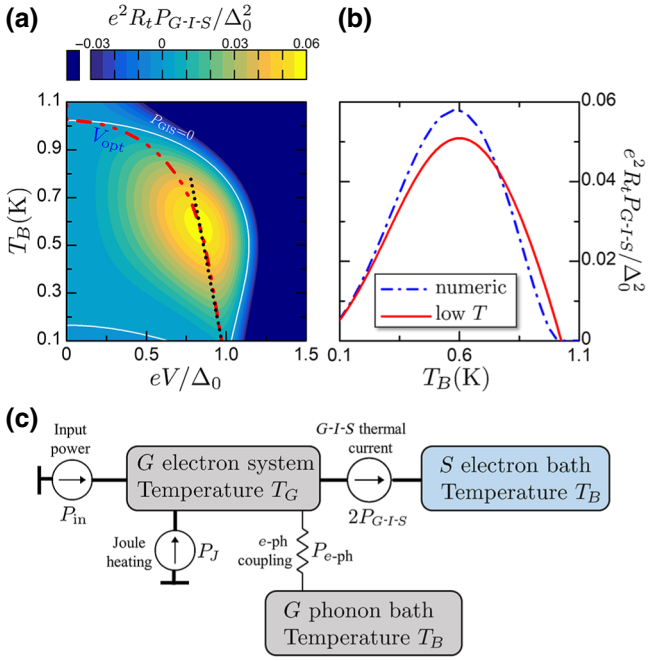

FIG. 2. Cooling characteristic of the G-I-S junction. (a) Heat current $P_{G\text{-}I\text{-}S}$ vs the single junction bias voltage V and the bath temperature T_B when $T_G = T_B$. When $P_{G\text{-}I\text{-}S} > 0$, the heat is extracted from the graphene. The solid white line indicates the boundary between the cooling and the heating regions. The red dot-dashed curve represents the optimal bias $V_{\rm opt}$ where $P_{G\text{-}I\text{-}S}$ is maximized for fixed T_B. The black dotted line $eV = \Delta_0 - 0.66k_BT_S$ is the low T_B approximation of $V_{\rm opt}$. (b) The value of $P_{G\text{-}I\text{-}S}$ at the optimal bias $V_{\rm opt}$, obtained by numeric integration of Eq. (5) or by the low T approximation in Eq. (7). (c) Thermal model of a S-I-G-I-S. The electron system at temperature T_G is under different heat currents. One is the heat exchange with the graphene phonon bath $P_{e\text{-ph}}$. At the same time, heat is pumped away by the junction with power $2P_{G\text{-}I\text{-}S}$ and released in the superconductor electron bath. Another source of heat is the Joule heating given by the flowing electric current.

cooling power is maximized, for given value of T_B, at the optimal voltage bias $V_{\rm opt}(T_B)$ [see the red curve in Fig. 2(a)]. The cooling power value along the $V_{\rm opt}$ curve is reported in Fig. 2(b) as a function of T_B. The maximum is about $P_{G\text{-}I\text{-}S} \approx 0.06\Delta_0^2/(e^2R_t)$ for $T_B \approx 0.6$ K $\approx T_c/2$ and $V \approx 0.82\Delta_0/e$ (approximately 170 μV for aluminum). For $R_t = 10$ kΩ, the maximum cooling power corresponds to about $P_{G\text{-}I\text{-}S} \approx 0.24$ pW.

Low-temperature $(T_S, T_G \ll \Delta_0/k_B)$ approximated expressions of Eqs. (4) and (5) are reported in Refs. [23,24,77,78]. In this approximation, the optimal cooling is $eV_{\rm opt} \approx \Delta_0 - 0.66k_BT_S$ [see the dotted black curve in Fig. 2(a)], corresponding to an electric current

$$I \approx 0.48\frac{\Delta_0}{eR_t}\sqrt{\frac{k_BT_G}{\Delta_0}}, \tag{6}$$

and a related cooling power

$$P_{G\text{-}I\text{-}S} \approx \frac{\Delta_0^2}{e^2R_t}\left[0.59\left(\frac{k_BT_G}{\Delta_0}\right)^{3/2} - \sqrt{\frac{2\pi k_BT_S}{\Delta_0}}e^{-\Delta_0/k_BT_S}\right]. \tag{7}$$

Before concluding this section, we wish to discuss the dependence of Eqs. (4) and (5) on the carrier density n and how this can affect the electronic and thermal transport. The carrier density n is tuned via field effect by the gate voltage V_G [see Fig. 1(a)]. The electric and thermal currents depend on n through the tunnel resistance R_t. The latter is proportional to the DOS of both graphene and superconductor and to the modulus square of the tunneling amplitude $|U_0|^2$, i.e., $R_t \propto 1/(\rho_{G0}\rho_{S0}|U_0|^2)$ [75,79]. Since $\rho_{G0} \propto \sqrt{n}$, the G-I-S tunnel resistance depends on the carrier density as

$$R_t(n) = R_t(n = n_0)\sqrt{\frac{n_0}{n}}, \tag{8}$$

where n_0 is the residual carrier density. This equation implies

$$I(V, T_G, T_S, n) = I(V, T_G, T_S, n = n_0)\sqrt{\frac{n}{n_0}}, \tag{9}$$

$$P_{G\text{-}I\text{-}S}(V, T_G, T_S, n) = P_{G\text{-}I\text{-}S}(V, T_G, T_S, n = n_0)\sqrt{\frac{n}{n_0}}. \tag{10}$$

This simple scaling on n is valid when the approximation $\rho(\epsilon - eV - E_F) \approx 1$, i.e., when $E_F \gg \Delta_0$. This condition is experimentally respected since charge density n can be tuned typically in a range from 5×10^{10} to 5×10^{13} cm^{-2}, when using standard solid gating. This range is experimentally limited on the bottom by the presence of charge puddles [68] and on the top by the occurrence of gate dielectric breakdown caused by high voltage.

B. *S-I-G-I-S* thermal model

In this section, we describe the thermal model that includes all the thermal channels to graphene, as sketched in Fig. 2(c). We consider the graphene sheet homogeneously at the same temperature, neglecting the spatial dependence of T_G, thanks to the high heat diffusivity in graphene [58–60]. Moreover, we treat the graphene phonon bath as a reservoir at a fixed temperature T_B. This assumption is physically reasonable owing to the negligible Kapitza thermal resistance between the graphene and the substrate [80,81]. Finally, we consider the superconductor electrons as a thermal reservoir well thermalized with the substrate, by imposing $T_S = T_B$. This assumption can be violated in real experiments, where the heat

pumped into the superconductor heats up its quasiparticles, and the weak electron-phonon coupling provides a poor cooling to the bath [23]. This effect is detrimental for the superconducting state and, as a consequence, for cooling. In general, this effect can be weakened by contacting the superconductor with hot quasiparticle traps or coolers in cascade [43–45,82,83], making our assumption physically reasonable. Moreover, in a *S-I-G-I-S* system, the amount of heat transferred into the superconductor is lower than that present in a *S-I-N-I-S* system, because of the lower heat leakage from the phonon bath to the graphene electrons.

Thus, in our thermal model [see Fig. 2(c)] the only variable is the graphene temperature T_G, which is determined by the solution of the following heat balance equation:

$$C(T_G)\frac{dT_G}{dt} + 2P_{G\text{-}I\text{-}S}(T_G, T_B, V) + P_{e\text{-ph}}(T_G, T_B) - P_J(T_G, T_B, V) = P_{\text{in}}. \tag{11}$$

This equation takes into account the heat current across the two junctions $2P_{G\text{-}I\text{-}S}$, the electron-phonon coupling in graphene $P_{e\text{-ph}}$, the Joule heating P_J and a possible external power input P_{in} (for example a radiation power) that we consider to investigate the bolometric response. We also consider the time dependence of T_G introducing the electron heat capacity C, which plays the role of thermal inertia of the system when dynamic response is investigated.

Let us consider the electron-phonon heat current $P_{e\text{-ph}}$. Below the Bloch-Grüneisen temperature (approximately 50 K), $P_{e\text{-ph}}$ is characterized by the presence of two different regimes depending on whether the wavelength of thermal phonons is longer or shorter than the electron mean free path l_{MFP} [47,48,84–86]. In the clean regime (or short wavelength regime) the *e*-ph coupling reads

$$P_{e\text{-ph}} = A\Sigma_C\left({T_G}^4 - {T_B}^4\right), \tag{12}$$

$$\Sigma_C = \frac{\pi^{5/2}D_p^2\sqrt{n}{k_B}^4}{15\rho_M\hbar^4 v_F^2 s^3}, \tag{13}$$

while in the dirty regime (or long wavelength regime) takes the form

$$P_{e\text{-ph}} = A\Sigma_D\left({T_G}^3 - {T_B}^3\right), \tag{14}$$

$$\Sigma_D = \frac{2\zeta(3)D_p^2\sqrt{n}k_B^3}{\pi^{3/2}\rho_M\hbar^3 v_F^2 s^2 l_{\text{MFP}}}, \tag{15}$$

where Σ_C, Σ_D are the electron-phonon coupling constants, depending on the sound speed $s \approx 2\times10^4$ m/s, the mass density $\rho_M \approx 7.6\times10^{-7}$ kg/m^2, the deformation potential $D_p \approx 13$ eV, $l_{\text{MFP}} \approx 60$ nm and the Riemann zeta $\zeta(3) \approx 1.2$. As a final result, the coupling constants are $\Sigma_C \approx 0.024$ pW μm^{-2} K^{-4} and $\Sigma_D \approx 0.023$ pW μm^{-2} K^{-3} [46–48,74,87–89].

In the following we consider both the graphene regimes, writing the generic coupling $P_{e\text{-ph}} = A\Sigma_\delta({T_G}^\delta - {T_B}^\delta)$, where δ can be 3 or 4 according to a dirty or clean regime, respectively, and Σ_δ is Σ_C or Σ_D coherently. In the temperature range between 0.1 and 1 K, graphene on SiO_2 shows a dirty regime, while the *h*-BN-encapsulated graphene is in a clean regime [47,74]. The reason is the different mobility (and therefore different electron mean free path) due to the presence of the *h*-BN encapsulation [47,48,74].

The effect of the two regimes can be evaluated by the electron-phonon thermal conductance $G_{e\text{-ph}}$ in a system where T_G is perturbed from the equilibrium. $G_{e\text{-ph}}$ is calculated by the linear expansion $P_{e\text{-ph}} \approx G_{e\text{-ph}}(T_G - T_B)$ where

$$G_{e\text{-ph}} = \left.\frac{\partial P_{e\text{-ph}}}{\partial T_G}\right|_{T_B} = \begin{cases} 3A\Sigma_D {T_B}^2, & \text{dirty regime,} \\ 4A\Sigma_C {T_B}^3, & \text{clean regime.} \end{cases} \tag{16}$$

The $G_{e\text{-ph}}$ in the two regimes are of the same order of magnitude at $T_B = 1$ K, but the different temperature scaling makes the clean regime weaker compared to the dirty one when T_B is below 1 K.

The Joule heating is due to the electron current flow in the resistive sheet of graphene. It is given by $P_J = R_G I^2(T_G, T_B, V)$ and is a component that spoils cooling. In this system, the current-voltage characteristic is nonlinear, and the current is suppressed by the presence of the superconductor gap. The Joule heating scales as $\Delta_0^2 R_G/(eR_t)^2$, while the cooling power as Δ_0^2/e^2R_t. The ratio between the Joule heating and the cooling power then scales as R_G/R_t, implying that the cooling performance is not affected by the Joule effect when $R_G \ll R_t$. Indeed, we find out in our simulations that Joule heating weakly affects the thermal equilibrium, which is instead dominated by the competition between $P_{G\text{-}I\text{-}S}$, $P_{e\text{-ph}}$, and P_{in}. For this reason, we neglect the Joule heating in the analytic results, while we keep it in the numerical ones.

We remark that, in our thermal model, we do not include the photonic and the phenomenological backtunneling channels [24,87,90–92]. These two contributions are indeed dependent on the fabrication parameters, such as the device design and on the junction quality. For this reason, they are often considered as empirical parameters to fit the experimental data. Moreover, in the range of temperatures studied in this paper (above 0.1 K), the photonic thermal conductance in our device is negligible compared to the phononic thermal conductance [87]. Finally, the quasiparticle backscattering can be managed by adjusting the tunnel resistance of the junction.

The heat capacity for $k_B T_G \ll E_F$ is given by the standard Fermi liquid result [87,88,93]

$$C = A\gamma T, \tag{17}$$

where $\gamma = (\pi^2/3)k_B^2\rho_{G0}$ is the Sommerfeld coefficient. We notice that the linear behavior of C in temperature is due to the fact that $k_B T_G \ll E_F$, yielding the same behavior of a metal. The dependence of C on the Fermi energy (and hence by the residual charge by $E_F = \hbar v_F\sqrt{\pi n}$) is contained in $\gamma \propto \rho_{G0}(E_F) \propto \sqrt{n}$.

Finally, we comment on the dependence of the heat current contributions on carrier density. For simplicity, we assume a homogeneous charge density n over the whole graphene area, even though under the metallic contacts the screening may slightly affect this assumption. Anyway, since cooling requires very small potential differences (approximately equal to 1 mV) between the contacts and graphene, the electron density under the electrodes can be considered constant. Hence, the carrier density of the whole graphene sheet can be tuned mainly by the backgate, with negligible charge inhomogeneities due to the specific electrostatic problem. We recall that the sheet resistivity is given by $\rho \propto 1/n$, implying

$$R_G(n) = R_G(n = n_0)\frac{n_0}{n}. \tag{18}$$

This equation and $R_t(n)$ in Eq. (8) return that $P_J \propto R_G/R_t^2$ does not depend on n. Moreover, considering Eq. (10) and $P_{e\text{-ph}} \propto \sqrt{n}$, the heat balance equation can be written as

$$\begin{aligned} &2\sqrt{\frac{n}{n_0}}P_{G\text{-}I\text{-}S}(T_G, T_B, V, n = n_0) \\ &\quad + \sqrt{\frac{n}{n_0}}P_{e\text{-ph}}(T_G, T_B, n = n_0) - P_J(T_G, T_B, V, n = n_0) \\ &\quad = P_{\text{in}} - \sqrt{\frac{n}{n_0}}C(T_G, n = n_0)\frac{dT_G}{dt}. \end{aligned} \tag{19}$$

The dominant terms $P_{G\text{-}I\text{-}S}$ and $P_{e\text{-ph}}$ scale as $\sqrt{n}$. The terms that are constant in n are the Joule heating and the external power input P_{in}. Hence, the thermal properties are weakly affected by the graphene carrier density if Joule heating is negligible and $P_{\text{in}} = 0$. The heat balance equation in the presence of an external source ($P_{\text{in}} \neq 0$) is discussed in Sec. V.

III. BASE TEMPERATURE

In this section, we investigate the stationary ($\partial_t T_G = 0$) quasiequilibrium case of the heat balance equation (11) in the absence of external input power ($P_{\text{in}} = 0$). Solving the balance equation for T_G, we can calculate the base temperature $T_{G,b}$ reached by cooled graphene.

Figure 3(a) reports a color map of $T_{G,b}/T_B$ vs (V, T_B) for the case of clean graphene regime. The black line for $T_G/T_B = 1$ separates the region of cooling and heating of graphene. Figure 3(b) reports T_G vs V for chosen values of bath temperature T_B. When $V \to 0$, the graphene temperature tends to the equilibrium with the bath temperature

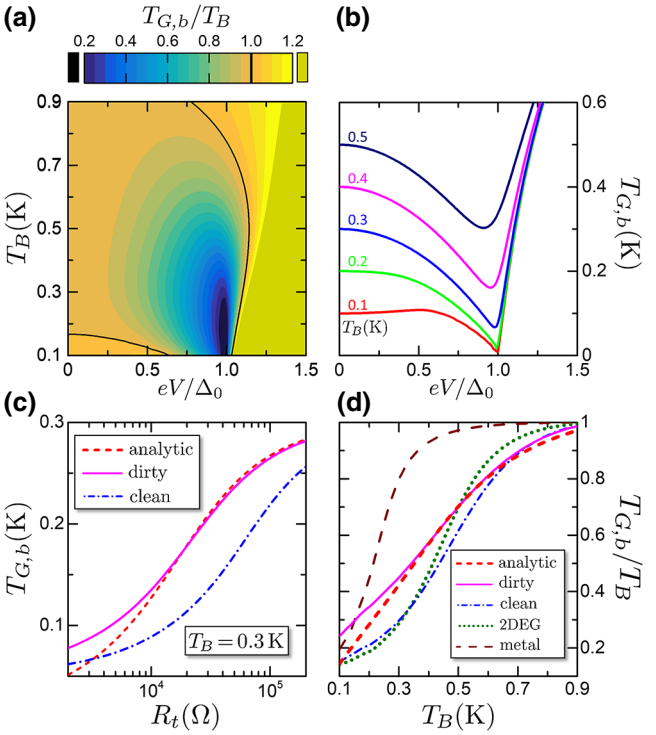

FIG. 3. (a) Color map of the ratio of the base temperature $T_{G,b}$ with the bath temperature T_B vs V and T_B in the clean electron-phonon regime. The black line shows $T_{G,b}/T_B = 1$ (no cooling) and delimits the region where cooling is present. (b) $T_{G,b}$ vs V for different bath temperatures T_B. (c) $T_{G,b}$ vs tunnel resistance R_t for fixed $T_B = 0.3$ K. The analytic curve plots Eq. (21). The other curves are calculated numerically for the case of graphene in dirty and clean regime. (d) Comparison of $T_{G,b}/T_B$ in different materials, for the same area A and tunnel resistance R_t. We plot the results for graphene in dirty and clean regime, the analytical result in Eq. (21) for dirty graphene, an ultrathin metal film of thickness 1 nm and a 2DEG in $In_{0.75}Ga_{0.25}As$.

T_B. The minimum temperature is reached when the voltage bias is set closely below $\Delta(T)/e$. In the dirty regime, the cooling behavior is qualitatively similar but lower in performance compared to that in the clean graphene regime, due to the stronger e-ph thermal conductance [see Eq. (16)], implying higher base temperatures.

When Joule effect is negligible, the base temperature is given by the equilibrium between the electron-phonon heating power and the junction-cooling power. The former scales as the area A, while the latter scales as $P_{G\text{-}I\text{-}S} \propto R_t^{-1}$. As a consequence, the base temperature is lowered by decreasing the factor AR_t. The junction resistance cannot be decreased at will since the $R_G \ll R_t$ condition must be satisfied; otherwise, the detrimental Joule heating contribution is not negligible, and the voltage partition between sheet and junctions must be properly considered.

The heat balance equation can be solved analytically at optimal bias and low temperatures if the Joule heating is negligible and if the graphene is in the dirty regime.

With these assumptions, Eq. (7) can be used for $P_{G\text{-}I\text{-}S}$ and then the heat balance equation has a polynomial form that can be solved exactly. On the other hand, the $T_G{}^4$ form of the e-ph coupling in clean regime yields a not analytically solvable balance equation. The analytic solution is obtained by substituting $P_{G\text{-}I\text{-}S}$ with Eq. (7) and $P_{e\text{-ph}}$ with Eq. (15) in the thermal balance equation $2P_{G\text{-}I\text{-}S} + P_{e\text{-ph}} = 0$, yielding

$$\frac{2\Delta_0^2}{e^2 R_t}\left[0.59\left(\frac{k_B T_G}{\Delta_0}\right)^{3/2} - \sqrt{\frac{2\pi k_B T_B}{\Delta_0}}e^{-\Delta_0/k_B T_B}\right] + A\Sigma_D(T_G{}^3 - T_B{}^3) = 0, \tag{20}$$

which is a second-order equation $y^2 + 2by - c = 0$ in $y = (k_B T_G/\Delta_0)^{3/2}$ and

$$b = \frac{0.59 k_B{}^3}{A\Sigma_D \Delta_0 e^2 R_t},$$
$$c = \left(\frac{k_B T_B}{\Delta_0}\right)^3 + \frac{2k_B{}^3}{A\Sigma_D\Delta_0 e^2 R_t}\sqrt{\frac{2\pi k_B T_B}{\Delta_0}}e^{-\Delta_0/k_B T_B},$$

with physical solution

$$T_{G,b} = \frac{\Delta_0}{k_B}\left(\sqrt{b^2 + c} - b\right)^{2/3}. \tag{21}$$

Figure 3(c) reports the dependence of $T_{G,b}$ on R_t calculated numerically in the case of dirty and clean regimes. The analytical result of Eq. (21) for $T_{G,b}$ in the dirty regime is represented by the red dashed line. We can notice that decreasing R_t further reduces the achievable base temperature. The agreement between the numeric and analytic results for $T_{G,b}$ in the dirty regime is generally good if $T_{G,b}/T_B \approx 1$. When $T_{G,b}/T_B \ll 1$, the solution depends on the accuracy of the $P_{G\text{-}I\text{-}S}$ approximation with the consequence that the leading-order approximation of $P_{G\text{-}I\text{-}S}$ in Eq. (7) is not anymore sufficient.

In order to investigate the advantage of graphene e-ph coupling, we make a comparison of the base graphene temperature in a S-I-G-I-S with the base temperature of a tunnel-cooled system based on a metallic thin film and a 2DEG. To this aim, we solve the balance equation $2P_{G\text{-}I\text{-}S} + \tilde{P}_{e\text{-ph}} = 0$ for the different systems, where $P_{G\text{-}I\text{-}S}$ is the same but $\tilde{P}_{e\text{-ph}}$ is the electron-phonon heat current in a metallic thin film or in a conventional 2DEG with parabolic band dispersion [94]. For simplicity, we neglect the resistances of metal and 2DEG and the related Joule heating. For the sake of comparison, we consider the same A and R_t. For a metallic thin film, it is $\tilde{P}_{e\text{-ph}} = Aw\Sigma_N(T_e^5 - T_B{}^5)$ and $\Sigma_N = 1$ nWμm^{-3}K^{-5}, where T_e is the electron temperature. We consider a low thickness $w = 1$ nm, for which we have a coupling per unit area $w\Sigma_N \approx 1$ pW μm^{-2}K^{-5}. For a 2DEG in $In_{0.75}Ga_{0.25}As$, we have $\tilde{P}_{e\text{-ph}} = A\Sigma_{2DEG}(T_e^5 - T_B{}^5)$ and a coupling per unit area $\Sigma_{2DEG} \approx 0.073$ pWμm^{-2}K^{-5} [94–96]. At a temperature of the order of 1 K, the coupling per unit area of the metal is about 40 times larger than that of graphene, while the coupling per unit area of the 2DEG is about three times larger. It can be expected that graphene and 2DEG can reach lower temperatures compared to the metallic thin film. This is shown in Fig. 3(d), reporting the base temperatures of the different systems.

Deeper insight can be reached by comparing the e-ph thermal conductance per unit area of the different systems. We have in a metal $G_N/A = 5w\Sigma_N T_B{}^4$, in a 2DEG $G_{2DEG}/A = 5\Sigma_{2DEG}T_B{}^4$ and in graphene $G_{e\text{-ph}}/A = \delta\Sigma_\delta T_B{}^{\delta-1}$, with δ indicating different e-ph regime. It can be noticed that the former two have a better scaling behavior compared to graphene. However, in metals, the coupling constant is large enough that this advantage is effective only below $T_B = 0.1$ K, i.e., below the typical temperature range for the tunnel cooling. This can be seen in Fig. 3(d) where the metal curve reaches the graphene curves (dirty and clean) at about 0.1 K. We remark that a 1-nm-thick metallic film is very challenging to be produced. A different conclusion holds for the 2DEG where the coupling constant Σ_{2DEG} is low enough that the T^5 scaling of $\tilde{P}_{e\text{-ph}}$ can allow for a lower e-ph heat current in the temperature interval of interest. This can be seen in Fig. 3(d), where the 2DEG reaches the base temperature of graphene at $T \approx 0.5$ K for dirty regime and at $T = 0.3$ K for clean regime. This indicates that cooling performances for a 2DEG and a S-I-G-I-S are comparable. In this case, the main (and nontrivial) advantage in graphene relies on the fabrication issues. Indeed, the growth of III–IV materials for 2DEGs requires molecular beam epitaxy that is an expensive technique. Furthermore, the use of 2DEGs implies the use of several steps of lithography, etching, and evaporation of metals. On the other hand, chemical vapor deposition is nowadays an established and cheaper technique for growing graphene or h-BN–G–h-BN heterostructures [73], allowing easier scalability to industrial standards.

IV. THERMAL RESPONSE DYNAMICS

In this section, we study the dynamics of the S-I-G-I-S with thermal perturbations from the base temperature, focusing on its response time. The latter is an important parameter for any time-dependent application since it affects the thermal bandwidth of the system.

The response time is a parameter that appears in the transfer functions and involves thermal properties, such as the power-to-temperature transfer function or the bolometric responsivity. Both these quantities are studied below.

As an example of thermal response, we report in Fig. 4 the numerical solution of the heat balance equation (11) at bath temperature $T_B = 0.5$ K, optimal voltage

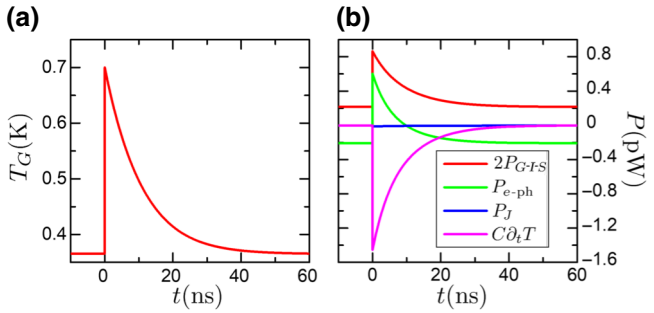

FIG. 4. (a) Time evolution of T_G after a power pulse that brings the graphene from $T_{G,b} \approx 0.37$ K to $T_G = 0.7$ K. Here the bath temperature is $T_B = 0.5$ K, V is at the optimal bias $eV \approx 0.87\Delta_0$ and the graphene is in dirty regime. (b) Time evolution of the heat current components in Eq. (11) corresponding to temperature in (a). The Joule component P_J is negligible compared to junction and electron-phonon components. At equilibrium, $2P_{G\text{-}I\text{-}S} \approx -P_{e\text{-ph}}$.

bias $eV_{\rm opt}(T_B) \approx 0.87\Delta_0$ and dirty graphene regime. Figure 4(a) shows the evolution of temperature over time. At $t < 0$, the graphene is at base temperature $T_{G,b} \approx 0.37$ K. The input power is null for the whole process, except at $t = 0$, where a power pulse drives the graphene temperature from $T_{G,b}$ to $T_G = 0.7$ K. After this pulse, the graphene thermalizes to the bath temperature in about 50 ns. The associated heat currents' evolution is plotted in Fig. 4(b). In the whole process, it is $2P_{G\text{-}I\text{-}S} + P_{e\text{-ph}} + C(T_G)\partial_t T_G = 0$. At $t < 0$, the graphene is in a stationary state, where $\partial_t T_G = 0$ and the equilibrium is given by $2P_{G\text{-}I\text{-}S} + P_{e\text{-ph}} = 0$. From Fig. 4(b) it can be noticed that the numerical calculations yield an always negligible Joule heating.

Important physical insight into the dynamics can be obtained by studying small perturbations from base temperature by linearizing the heat balance equation. Therefore, we consider the left-hand side of Eq. (11) in a series expansion around $T_G = T_{G,b}$ and we assume a constant heat capacity for small perturbations: $C(T) \approx C(T_{G,b})$. Moreover, we neglect Joule heating. In this way, we have the linearized thermal equation

$$C\frac{d\Delta T_G}{dt} + (2G_{G\text{-}I\text{-}S} + G_{e\text{-ph}})\Delta T_G = 0, \tag{22}$$

where $\Delta T_G = T_G - T_{G,b}$, and $G_{G\text{-}I\text{-}S}$ and $G_{e\text{-ph}}$ are thermal conductances related to the junction and the e-ph coupling, respectively. The first term is

$$\begin{aligned} G_{G\text{-}I\text{-}S} &= \left.\frac{\partial P_{G\text{-}I\text{-}S}}{\partial T_G}\right|_{T_{G,b}} \\ &= \frac{1}{e^2 R_t}\int_{-\infty}^{\infty} d\epsilon \left\{ \frac{(\epsilon - eV)^2}{4k_B {T_{G,b}}^2} \frac{1}{\cosh^2\left(\frac{\epsilon - eV}{2k_B T_{G,b}}\right)} \right. \\ &\quad \left. \times\ \rho_G(\epsilon - eV - E_F)\rho_S(\epsilon) \right\} \\ &\approx \frac{3 \times 0.59}{2}\frac{\Delta_0 k_B}{e^2 R_t}\left(\frac{k_B T_{G,b}}{\Delta_0}\right)^{1/2}, \end{aligned} \tag{23}$$

where the approximation in the last passage is valid at $V_{\rm opt}$ and $T_B, T_G \ll \Delta_0/k_B$. The e-ph channel $G_{e\text{-ph}}$ is given by Eq. (16) evaluated at the equilibrium point $T_G = T_{G,b}$.

The solutions of the linearized thermal balance equation (22) have the exponential form $\Delta T_G \propto e^{-t/\tau_{\rm th}}$, where $\tau_{\rm th}$ is the response time at $V_{\rm opt}$ given by

$$\tau_{\rm th} = \frac{C}{G_{\rm tot}} \approx \frac{A\gamma T_{G,b}}{\delta A \Sigma_\delta {T_{G,b}}^{\delta-1} + 1.8\frac{\Delta_0 k_B}{e^2 R_t}\left(\frac{k_B T_{G,b}}{\Delta_0}\right)^{1/2}}. \tag{24}$$

The denominator in Eq. (24) is the sum of the junction and e-ph thermal conductances. The different temperature scaling of $G_{G\text{-}I\text{-}S}$ and $G_{e\text{-ph}}$ implies two regimes defined by the dominance of one of the two channels. The two regimes are separated by a crossover temperature $T_{G,\rm cr}$ that can be estimated by equation $G_{G\text{-}I\text{-}S}(T_{G,b}) = G_{e\text{-ph}}(T_{G,b})$, yielding

$$T_{G,\rm cr} = \left(\frac{1.8\Delta_0^{1/2} {k_B}^{3/2}}{e^2 R_t \delta A \Sigma_\delta}\right)^{1/(\delta - 1.5)}. \tag{25}$$

We obtain $T_{G,\rm cr} = 0.39$ K for dirty graphene regime and $T_{G,\rm cr} = 0.53$ K for clean graphene regime. When $T_{G,b} \ll T_{G,\rm cr}$ the junction conductance dominates over the e-ph conductance and $\tau_{\rm th}$ is

$$\tau_{\rm th} \sim \frac{A\gamma e^2 R_t}{1.8{k_B}^2}\left(\frac{k_B T_{G,b}}{\Delta_0}\right)^{1/2}. \tag{26}$$

For $T_{G,b} \gg T_{G,\rm cr}$, there is a regime dominated by the e-ph coupling, yielding

$$\tau_{\rm th} \sim \frac{\gamma {T_{G,b}}^{2-\delta}}{\delta \Sigma_\delta}, \tag{27}$$

which depends only on the graphene properties and not on geometrical parameters of the *S-I-G-I-S*.

Figure 5(a) shows the dependence of $\tau_{\rm th}$ on T_B at optimal voltage bias for different values of R_t. The solid lines correspond to Eq. (24) where $T_{G,b}$ is given by Eq. (21). The dashed lines are obtained by numerically solving the heat balance equation when perturbing the graphene base temperature T_G of 10%. The numerical and analytical results are in good agreement. The maximum of each curve is the crossover point between the two regimes dominated by the junction [Eq. (26)] and the e-ph coupling [Eq. (27)]. The response time increases with R_t, since the thermal

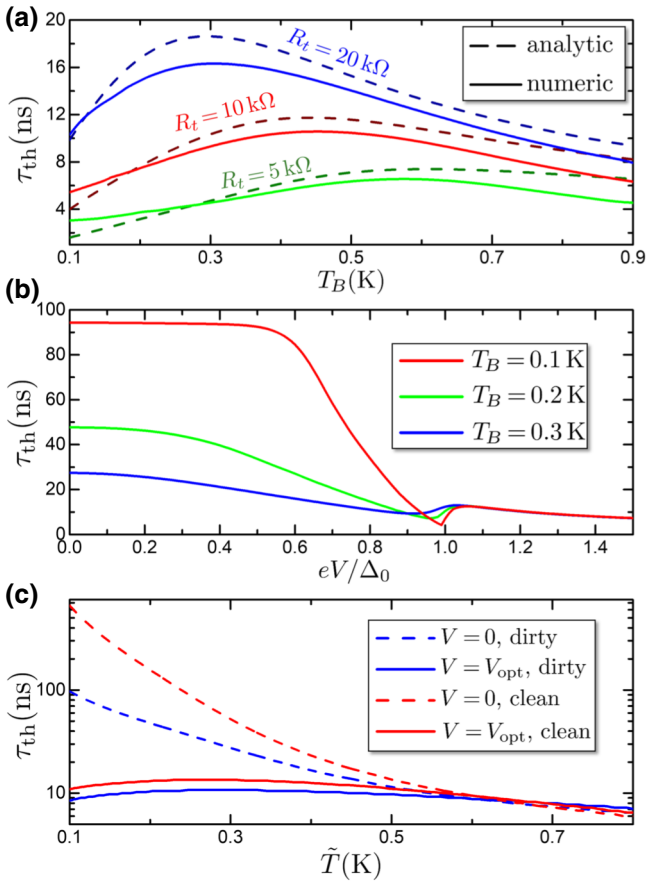

FIG. 5. (a) Response time τ_{th} vs T_B at the optimal bias for a system with dirty graphene regime and different tunnel resistances R_t, numerical and analytical [see Eq. (24)]. (b) τ_{th} vs V for $T_B = 0.1$ K, 0.3 K, 0.5 K. (c) τ_{th} vs $\tilde{T}$ in a system where $(V = 0, T_G = T_B = \tilde{T})$ (dashed curves) and in a system where $(V = V_{\mathrm{opt}}, T_{G,b} = \tilde{T}, T_B{}')$ where $T_B{}'$ is such that $T_{G,b} = \tilde{T}$ (solid curves).

conductance of the junction is lowered. In particular, at low T_B, the curves of Fig. 5(a) indicate that $\tau_{\mathrm{th}} \propto R_t$ as given by Eq. (26).

The results in Eq. (24) and Fig. 5(a) are obtained for $V = V_{\mathrm{opt}}$. τ_{th} has a dependence also on the bias voltage, since the latter tunes the transport properties of the junction. Figure 5(b) reports τ_{th} vs V calculated for different bath temperatures in the case of dirty graphene regime. We notice that the response time τ_{th} decreases from 95 ns at $V = 0$ to 5 ns at $V = V_{\mathrm{opt}}$ when $T_B = 0.1$ K, because when the cooling operates, the junction thermal conductance is enhanced.

This point can be investigated analytically. To evaluate the voltage dependence of the thermal response at small bias, we need the thermal conductance of the junction $G_{G\text{-}I\text{-}S}(T_G = T_B, V = 0) = \partial_{T_G} P_{G\text{-}I\text{-}S}(T_G = T_B, V = 0)$. It can be approximated by the tunnel integral expression in Eq. (23) at $k_B T_G, k_B T_B \ll \Delta_0$. At the leading order we obtain finally

$$G_{G\text{-}I\text{-}S}(T_G, V = 0) \sim \frac{\sqrt{2\pi}\,\Delta_0 k_B}{e^2 R_t} \left(\frac{k_B T_G}{\Delta_0}\right)^{-3/2} e^{-\Delta_0/k_B T_G}. \tag{28}$$

Linearizing the heat balance equation around the equilibrium state $(T_G = T_B, V = 0)$ we obtain

$$\tau_{\mathrm{th}} = \frac{C}{G_{\mathrm{tot}}} \approx \frac{A\gamma T_{G,b}}{\delta A \Sigma_\delta {T_{G,b}}^{\delta-1} + G_{G\text{-}I\text{-}S}(T_G = T_B, V = 0)}. \tag{29}$$

The difference between $\tau_{\mathrm{th}}(V = 0)$ [Eq. (28)] and $\tau_{\mathrm{th}}(V = V_{\mathrm{opt}})$ [Eq. (23)] is strong. In particular, at low temperatures the junction conductance is exponentially suppressed at zero bias, while $G_{G\text{-}I\text{-}S}$ has a large contribution in the optimally biased case.

The difference of τ_{th} between the biased and unbiased case is remarked in Fig. 5(c). Dashed curves show τ_{th} in an unbiased system at $(T_G = T_B = \tilde{T}, V = 0)$, while solid curves show τ_{th} for $T_{G,b} = \tilde{T}$ and $T_B, V_{\mathrm{opt}}(T_B)$ are set subsequently. For completeness, we show both the dirty (blue curves) and clean (red curves) graphene regimes. The difference in response time between $V = 0$ and $V = V_{\mathrm{opt}}$ can reach 1 or 2 orders of magnitude depending on the value of T_G and the graphene regime. Furthermore, at $V = 0$, there is no maximum in τ_{th}, since both the $G_{e\text{-ph}}$ and $G_{G\text{-}I\text{-}S}$ are increasing functions of T_G.

It is worthwhile to note that the response time does not depend on carrier density n. Indeed, both C and G_{tot} are proportional to $\sqrt{n}$. As a consequence, the gating does not affect τ_{th}.

Finally, we evaluate the temperature response to a finite external power signal $P_{\mathrm{in}} \neq 0$. This quantity is exploited below for investigating the bolometric response of the device. It is useful to write the linear heat balance equation (22) in the frequency domain including the signal $P_{\mathrm{in}}(\omega)$. We remark that the frequency ω of P_{in} refers to the Fourier component of the power and not to the electromagnetic frequency. The resulting equation takes the form

$$\Delta T_G(\omega) = \mathcal{T}_{TP}(\omega) P_{\mathrm{in}}(\omega) = \frac{1}{G_{\mathrm{tot}}(1 + i\omega\tau_{\mathrm{th}})} P_{\mathrm{in}}(\omega), \tag{30}$$

where $\mathcal{T}_{TP} = 1/[G_{\mathrm{tot}}(1 + i\omega\tau_{\mathrm{th}})]$ is the power-to-temperature transfer function. This equation shows that the *S-I-G-I-S* responds as a low-pass filter with cutoff frequency $\omega_0 = 1/\tau_{\mathrm{th}}$. Considering the values of τ_{th} reported in Fig. 5(a), the corresponding frequency is in a range of 10–60 MHz. In the following section, this transfer function is used to evaluate the responsivity, a figure of merit that quantifies the *S-I-G-I-S* performances as a bolometer.

V. BIASED *S-I-G-I-S* AS A BOLOMETER

In this section, we study the cooled *S-I-G-I-S* as a bolometer. An input power $P_{\rm in}$ is converted in a variation of current when the *S-I-G-I-S* is kept at a constant voltage bias. In detail, we characterize two bolometric figures of merit, the responsivity, and the NEP.

The bolometric properties of a *S-I-N-I-S* system with electron cooling have been studied in the literature [54, 55,57,97]. The main result is that the built-in refrigeration enhances the responsivity and decreases the NEP. Here, we essentially follow a similar analysis for a *S-I-G-I-S*.

We point out that *S-I-G-I-S* systems have already been investigated in the literature, at $V \to 0$, where the cooling is negligible [14,74,98]. The purpose of these low V schemes is to decrease the thermal conductance across the junction in order to use the device at lower input power regimes [14,74,98].

Our bolometer scheme consists of a *S-I-G-I-S* system connected to an external voltage generator $V_{\rm ext} = 2V$, V being the voltage drop across a single junction [see sketch in Fig. 6(a)]. The graphene is also connected to the superconducting antenna by means of a clean superconductor-graphene junction. The superconducting antenna allows carrying the power $P_{\rm in}$ and traps it in graphene since the superconducting leads work as Andreev mirrors [52,54], reducing the thermal leakage to the antenna. It is important to remark that the distance between the antenna electrodes must be enough to make the Josephson coupling through proximity effect negligible [99]. The electric current I in the circuit is measured by means of an inductance coupled to a superconducting interferometer readout [9,11,12,100,101].

A. Responsivity

We start our investigation with the responsivity, defined as a power-to-current transfer function:

$$\mathcal{R}(\omega) = \frac{\partial I(\omega)}{\partial P_{\rm in}(\omega)}, \tag{31}$$

where $I(\omega)$ and $P_{\rm in}(\omega)$ are the electric current and the input power signal in the frequency domain, respectively.

We calculate the responsivity as the product of the power-to-temperature transfer function $\mathcal{T}_{TP}$ in Eq. (30) with the temperature-to-current transfer function $\mathcal{T}_{IT} = \partial_{\Delta T_G} I$. The product of the two transfer functions is equivalent to calculate the derivative $\mathcal{R} = \partial_{P_{\rm in}} I$ by the factorization $\mathcal{R} = \partial_{T_G} I \times (\partial_{T_G} P_{\rm in})^{-1}$, since $\mathcal{T}_{TP} = \partial_{P_{\rm in}} \Delta T$ [54]. We obtain

$$\mathcal{R}(\omega) = \mathcal{T}_{IT}(\omega)\mathcal{T}_{TP}(\omega) = \frac{\partial I/\partial T_G}{G_{\rm tot}(1 + i\omega\tau_{\rm th})} P_{\rm in}(\omega). \tag{32}$$

The responsivity has a cutoff at the frequency $\omega_0 = 1/\tau_{\rm th}$.

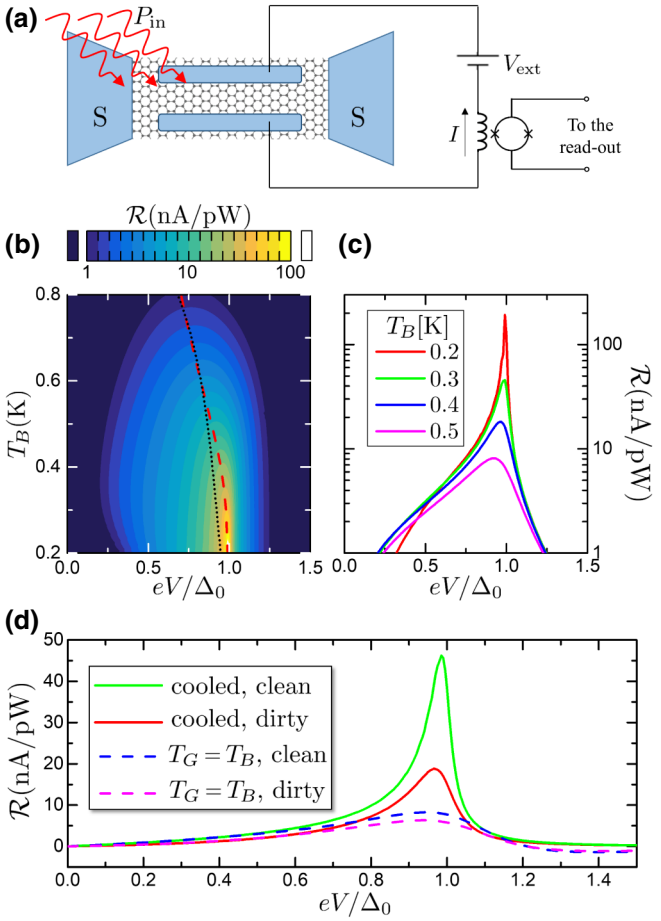

FIG. 6. (a) Bolometric detection scheme for the *S-I-G-I-S* system. The graphene is in clean contact with a superconducting antenna. A photonic power $P_{\rm in}$ increases the temperature of the electrons in graphene and changes the tunneling rate across the *G-I-S* junctions, resulting in a variation of the current I. The current is detected and amplified by a superconducting interferometer. (b) Color map of the responsivity $\mathcal{R}$ vs (V, T_B). (c) Cuts from (b) for the chosen temperatures in the legend. (d) $\mathcal{R}$ in the cases of dirty and clean graphene regime, in the presence of cooling or for $T_G = T_B$ (inefficient cooling), see the legend. The curves are obtained at $T_B = 0.3$ K.

We focus on the low frequency limit, which is valid when the band of the input signal is sufficiently below the cutoff frequency. Figure 6(b) reports a color map of $\mathcal{R}$ vs V and T_B, obtained by Eq. (32) using the numerical derivative of Eqs. (4) and (5). Cuts of Fig. 6(b) vs V are reported in Fig. 6(c). The responsivity shows a peak on the red dashed curve $V^{\mathcal{R}}_{\rm opt}(T_B)$. The latter does not coincide with $V_{\rm opt}$ [dotted black in Fig. 6(b)], which maximizes the cooling performances. Indeed, $V^{\mathcal{R}}_{\rm opt}(T_B)$ and $V_{\rm opt}$ are different by definition, since the former is obtained by maximizing $\partial_{T_G} I/\partial_{T_G} P_{\rm in}$ and the latter by maximizing $P_{G\text{-}I\text{-}S}$. $V^{\mathcal{R}}_{\rm opt}(T_B)$ is located closely below $\Delta(T_B)/e$. Above this voltage, the current characteristics $I(V, T_G, T_B)$ lose sensitivity to temperature since they converge to the Ohmic

behavior $I = V/R_t$. On the other hand, for V well below the gap, the current is suppressed.

Other physical features of responsivity are represented in Fig. 6(d). Here, the solid curves are calculated by considering the graphene cooling, while the dashed curves are obtained by imposing $T_{G,b} = T_B$, i.e., disregarding the cooling effect. This treatment corresponds to a physical situation where a spurious heating source completely spoils the cooling power of the junction. Let us investigate how the difference of graphene regime affects the responsivity. We first consider the dashed curves in Fig. 6(d), representing the absence of cooling, where we can notice that the clean case is slightly more responsive. The reason is due to the enhanced power-to-temperature transfer function $\mathcal{T}_{TP}$. Indeed, in both the dashed results ($T_{G,b} = T_B$), the temperature to current transfer function $\mathcal{T}_{IT}$ in Eq. (32) is the same, since it is a property of the junction depending only on V, T_G, and T_B. But the transfer function $\mathcal{T}_{TP}$ changes between a clean or dirty graphene regime, since the phonon thermal conductance is lower in the clean case. This means that, given a power input, the temperature raise ΔT_G is bigger in the clean case, resulting in a greater current response.

The comparison between the dashed and solid curves in Fig. 6(d) shows that the presence of an active cooling enhances the responsivity. The graphene base temperature is lower for clean graphene regime (see Sec. III), resulting in a stronger enhancement of responsivity compared to the dirty graphene case.

A physical insight to this argument can be obtained by using the low-temperature approximations studied above. We underline that these expressions hold for $V_{\rm opt}$ and not ${V_{\rm opt}}^{\mathcal{R}}$, but they give enough information for a physical picture. The responsivity at low temperatures is

$$\mathcal{R} = \frac{0.24\frac{k_B}{eR_t}\left(\frac{k_B T_{G,b}}{\Delta_0}\right)^{-1/2}}{\delta A \Sigma_\delta {T_{G,b}}^{\delta-1} + 1.8\frac{\Delta_0 k_B}{e^2 R_t}\left(\frac{k_B T_{G,b}}{\Delta_0}\right)^{1/2}}. \tag{33}$$

As in the previous section, the denominator shows the presence of two regimes separated by the crossover temperature $T_{G,\rm cr}$ in Eq. (25). The regime at $T_{G,b} \gg T_{G,\rm cr}$ is dominated by the e-ph thermal channel with responsivity

$$\mathcal{R} \approx \frac{0.24\sqrt{k_B\Delta_0}}{eR_t\delta A\Sigma_\delta {T_{G,b}}^{\delta-0.5}}. \tag{34}$$

The regime at $T_{G,b} \ll T_{G,\rm cr}$ is dominated by the junction thermal channel with responsivity at $V_{\rm opt}$

$$\mathcal{R} \approx 0.13\frac{e}{k_B T_{G,b}} \approx \frac{0.15}{T_{G,b}[\rm K]}\frac{\rm nA}{\rm pW}. \tag{35}$$

This expression does not involve any graphene property, but it is obtained by the ratio of the two junction properties $\partial_{T_G} I$ and $G_{G\text{-}I\text{-}S} = \partial_{T_G} P_{G\text{-}I\text{-}S}$. In particular, both terms scale as $1/R_t$, so the tunnel resistance does not directly affect the responsivity at low temperatures.

Finally, we stress that the responsivity increases by decreasing the graphene temperature. This is also confirmed by Figs. 6(b) and 6(c).

B. Noise equivalent power

We now focus on the noise equivalent power, which is defined as the signal power necessary to have a signal-to-noise ratio equal to 1 with a bandwidth of 1 Hz [102].

The total NEP of the *S-I-G-I-S* is given by different contributions [54]

$$\mathcal{N}^2_{\rm tot} = 2\mathcal{N}^2_{G\text{-}I\text{-}S} + \mathcal{N}^2_{e\text{-ph}} + \mathcal{N}^2_{\rm amp}, \tag{36}$$

where the three terms are related to the junction, the e-ph coupling and the amplifier readout, respectively. The factor 2 in front of $\mathcal{N}^2_{G\text{-}I\text{-}S}$ takes into account the two junctions, assuming their noises to be uncorrelated [103], which is related to the fact that temperature fluctuations, as the one induced by heat noise, are small in comparison to the stationary value of T_G [20].

The contribution to the junction NEP is given by fluctuations in both the electric and heat currents:

$$\mathcal{N}^2_{G\text{-}I\text{-}S} = \langle P^2\rangle - 2\frac{\langle IP\rangle}{\mathcal{R}} + \frac{\langle I^2\rangle}{\mathcal{R}^2}, \tag{37}$$

where the quantities in angled brackets are the low-frequency spectral densities of fluctuations [54]. $\langle I^2\rangle$ is the current fluctuation given by Ref. [54]

$$\langle I^2\rangle = \frac{2}{R_t}\int_{-\infty}^{\infty} d\epsilon\ \{\rho_G(\epsilon - eV - E_F)\rho_S(\epsilon)[f\,(\epsilon - eV, T_G) + f\,(\epsilon, T_S) - 2f\,(\epsilon - eV, T_G)f\,(\epsilon, T_S)]\}. \tag{38}$$

The fluctuation of the tunneling rate is mirrored in a fluctuation $\langle P^2\rangle$ of the tunneled heat

$$\langle P^2\rangle = \frac{2}{e^2R_t}\int_{-\infty}^{\infty} d\epsilon\ \{(\epsilon - eV)^2\rho_G(\epsilon - eV - E_F)\rho_S(\epsilon) \times [f\,(\epsilon - eV, T_G) + f\,(\epsilon, T_S) - 2f\,(\epsilon - eV, T_G) \times f\,(\epsilon, T_S)]\}. \tag{39}$$

Since the two fluctuations $\langle I^2\rangle$ and $\langle P^2\rangle$ are given by the tunneling of the same carriers, a non-null correlation exists [54]:

$$\langle IP\rangle = \frac{2}{eR_t}\int_{-\infty}^{\infty} d\epsilon\ \{(\epsilon - eV)\rho_G(\epsilon - eV - E_F)\rho_S(\epsilon) \times [f\,(\epsilon - eV, T_G) + f\,(\epsilon, T_S) - 2f\,(\epsilon - eV, T_G) \times f\,(\epsilon, T_S)]\}. \tag{40}$$

In these integrals, the energy dependence of graphene is neglected, according to the approximation done in Sec. II.

Figure 7 reports the NEP components for $T_S = T_B = 0.3$ K. Panel (a) shows the contributions to $\mathcal{N}_{G\text{-}I\text{-}S}$ in Eq. (37). For completeness, the NEP calculated by neglecting the cross-correlation between $\langle I^2 \rangle$ and $\langle P^2 \rangle$ is also reported

$$\mathcal{N}_{\rm unc} = \langle P^2 \rangle + \frac{\langle I^2 \rangle}{\mathcal{R}^2}. \tag{41}$$

By comparing $\mathcal{N}_{\rm unc}$ and $\mathcal{N}_{G\text{-}I\text{-}S}$ we can notice that the $\langle IP \rangle$ term brings a correction that reduces the total NEP. The cross-correlation is positive except in the region above the gap voltage $\Delta/e + 0.6 k_B T_G/e < V < \Delta/e + 1.3 k_B T_G/e$. Outside this region, the cross-correlation partially cancels the shot noise and the heat noise [54].

The NEP due to the junction noise is smaller in a *S-I-G-I-S* bolometer compared to a *S-I-N-I-S* bolometer. Indeed, $\mathcal{N}_{G\text{-}I\text{-}S}$ scales as ${R_t}^{-1/2}$ and good cooling characteristics can be reached in a *S-I-G-I-S* with a tunnel resistance one order of magnitude greater compared to a *S-I-N-I-S*. As a consequence, the $\mathcal{N}_{G\text{-}I\text{-}S}$ is lower of a factor approximately 3.

Let us consider the other NEP contributions. The contribution related to the noise in the *e*-ph channel can be roughly estimated by a generalization of expression in Ref. [54]

$$\mathcal{N}^2_{e\text{-ph}} = 2\delta k_B A \Sigma_\delta ({T_{G,b}}^{\delta+1} + {T_B}^{\delta+1}). \tag{42}$$

At equilibrium $T_G = T_B = T$, the NEP takes the standard form $\mathcal{N}^2_{e\text{-ph}} = 4 k_B G_{e\text{-ph}} T^2$ [14,74]. We notice that this term is smaller in a *S-I-G-I-S* compared to a *S-I-N-I-S*, due to the lower *e*-ph coupling constant (see discussion in Sec. III). In the temperature range of 0.1–1 K, the *e*-ph thermal conductance is 1 order of magnitude lower, yielding a $\mathcal{N}_{e\text{-ph}}$ decrease of a factor approximately 3.

Finally, we consider the readout NEP due to the amplifier noise $\langle I^2 \rangle_{\rm amp}$

$$\mathcal{N}^2_{\rm amp} = \frac{\langle I^2 \rangle_{\rm amp}}{\mathcal{R}^2} \tag{43}$$

and we assume $\sqrt{\langle I^2 \rangle_{\rm amp}} \approx 0.05\,{\rm pA}/\sqrt{\rm Hz}$ [54].

Figure 7(b) shows the different contributions to the total NEP at $T_B = 0.3$ K vs V. Panels (a) and (b) show the same $\mathcal{N}_{\rm GIS}$. We notice that $\mathcal{N}_{\rm tot}$ has a minimum close to the optimal bias. Here, the three contributions are of the same order of magnitude and yield $\mathcal{N}_{\rm tot} = 1.6 \times 10^{-18}\ {\rm W}/\sqrt{\rm Hz}$. Away from the optimal point, the readout $\mathcal{N}_{\rm amp}$ dominates. Hence, in order to optimize the total NEP, it is important to reduce the noise of the measurement circuitry.

The electronic cooling influences the NEP in two ways: on one side, it decreases the thermal fluctuations of electrons in graphene, on the other it enhances the responsivity [see Fig. 7(b)]. The former effect is quantified by the low-temperature expressions $V_{\rm opt}$ $\langle I^2 \rangle \approx (k_B T_{G,b})^{1/2} \sqrt{\Delta_0}/eR_t$, $\langle IP \rangle \approx (k_B T_{G,b})^{3/2} \sqrt{\Delta_0}/eR_t$, $\langle P^2 \rangle \approx (k_B T_{G,b})^{5/2} \sqrt{\Delta_0}/e^2 R_t$ [54]. The latter effect involves all the contributions that have $\mathcal{R}$ at the denominator. This is remarked by the total NEP vs (V, T_B) shown in Figs. 7(c) and 7(d), which resembles the inverse of responsivity in Figs. 6(b) and 6(c). In particular, the NEP improves of about 2 orders of magnitude moving from the zero-bias to the optimal-bias configuration.

We now investigate the effects of the carrier density n on the bolometric properties. The responsivity is not affected by n, since $\mathcal{T}_{TP} \propto G_{\rm tot}^{-1} \propto n^{-1/2}$ and $\mathcal{T}_{IT} \propto {R_t}^{-1} \propto n^{1/2}$. The term $\mathcal{N}_{G\text{-}I\text{-}S} \propto {R_t}^{-1/2} \propto n^{1/4}$ and similarly $\mathcal{N}_{e\text{-ph}} \propto \Sigma_\delta^{1/2} \propto n^{1/4}$. The readout term instead does not depend on n. Hence, the NEP is a weakly increasing function of n. Considering that the gating can vary n from the residual charge n_0 of a factor 100 at most, the NEP can vary of a factor approximately 3. Therefore, the bolometric

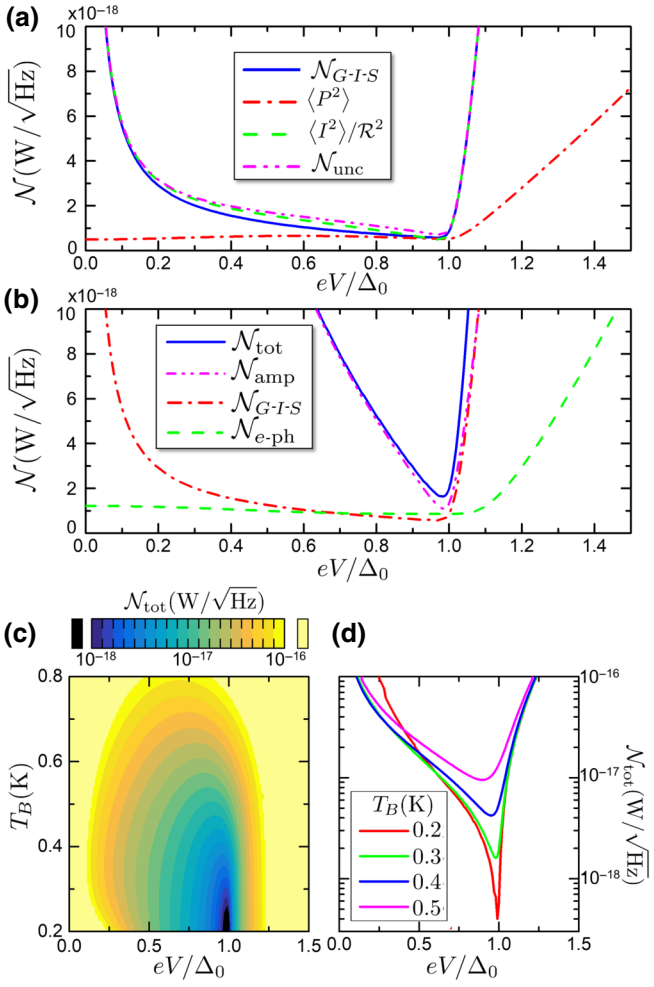

FIG. 7. (a) NEP components in a *G-I-S* junction at $T_B = 0.3$ K (clean graphene regime). (b) NEP components to the total NEP (clean graphene regime). (c) NEP color map vs V and T_B. (d) NEP cuts from (c) at bath temperatures T_B in the legend.

properties can be considered stable under charge variations or fluctuations.

VI. DEPENDENCE ON DYNES PARAMETER

Let us discuss here the role of the Dynes parameter, introduced in Eq. (3). This phenomenological parameter takes into account the finiteness of the superconducting peaks and the subgap tunneling [104]. The latter strongly depends on different issues, e.g., the fabrication quality of the junction [105] and, more generally, on environmental effects [106]. For this reason, Γ_D is frequently used as a parameter to quantify the quality of a tunnel junction with a superconductor. Indeed, realization of high-quality tunnel junctions is an important requirement to avoid effective subgap conduction channels. The value of Γ_D can be extracted experimentally from a fit of the measured electrical differential conductance $G_e(V)$ at low temperature $k_B T_G, k_B T_B \ll \Delta_0$, where $G_e(V) \propto \rho_S(eV)$.

The subgap density of states is

$$\rho_S(\epsilon < \Delta_0) \simeq \frac{\Gamma_D}{\Delta_0}, \tag{44}$$

which implies that for $eV, k_B T_G, k_B T_B \ll \Delta_0$ the junction behaves as a normal-metal-insulator-normal metal with effective resistance $\tilde{R}_t = R_t \Delta_0 / \Gamma_D$, with current $I \simeq V/\tilde{R}_t$ and Joule heating $V^2/\tilde{R}_t$.

In the previous sections, we assumed good-quality junctions with $\Gamma_D = 10^{-4}\Delta_0$. Such a value of Γ_D has been experimentally realized in metallic *N-I-S* junction, while it has not been reached in graphene junctions yet. Quality of *G-I-S* junctions is improved over time, and it can be nowadays expressed by Γ_D on the order of $10^{-1}\Delta_0$. State-of-the-art experiments hint that $\Gamma_D \approx 7 \times 10^{-2}\Delta_0$ [47].

In this section, we show how the Dynes parameter affects cooling and bolometric characteristics.

Effects on cooling. The cooling power is reduced by the increasing of the Dynes parameter since the smearing of the peaks in the BCS Dynes DOS does not allow sharp filtering of the hot electrons [23,24,107]. Moreover, the subgap conduction implies a Joule heating $V^2/\tilde{R}_t$, half of which flows in graphene. Figure 8(a) shows the cooling power $P_{G\text{-}I\text{-}S}$ vs the bias for different values of Γ_D, at the temperature $T_G = T_B = 0.5$ K. Up to $\Gamma_D = 10^{-2}\Delta_0$, the cooling power is slightly affected by Γ_D. From $\Gamma_D = 10^{-2}\Delta_0$ to $\Gamma_D = 10^{-1}\Delta_0$, the cooling power is strongly decreased. This is mirrored in the graphene base temperature $T_{G,b}$. Figure 8(b)–(d) show $T_{G,b}/T_B$ vs the bias V and the bath temperature T_B, for $\Gamma_D/\Delta_0 = 0.05, 10^{-2}, 10^{-3}$, respectively. In particular, the region of (V, T_B) where the temperature is decreased depends on Γ_D. Anyway, the simulations suggest that cooling can still be observed for $\Gamma_D = 0.05\Delta_0$, where $T_{G,b}/T_B$ can reach the value of approximately 0.8. For $\Gamma_D = 10^{-2}\Delta_0$, the cooling is well operating. For $\Gamma_D = 10^{-3}\Delta_0$, the $T_{G,b}/T_B$ plot resembles the one in Fig. 3(a).

Effects on the response time. The value of $\tau_{\rm th}$ is weakly affected by Γ_D at $V_{\rm opt}$. Indeed, when the junction is biased, the subgap contribution to the thermal conductance plays a marginal role compared to the contribution of the states above the gap. In Fig. 8(e), we report instead what happens at finite bias, plotting $\tau_{\rm th}$ at $T_B = 0.1$ K vs V for different values of Γ_D. At $eV \sim \Delta_0$, the response time is weakly affected by Γ_D, keeping on the order of 10 ns. The response time is affected by Γ_D only around $V \sim 0$ and at low temperatures $T_G, T_B \lesssim 0.2$ K, since the contribution of the subgap conduction and the electron-phonon coupling are comparable. Anyway, we remark that for $T_G, T_B \gtrsim 0.2$ K, the dependence on Γ_D is negligible, independently on the bias V.

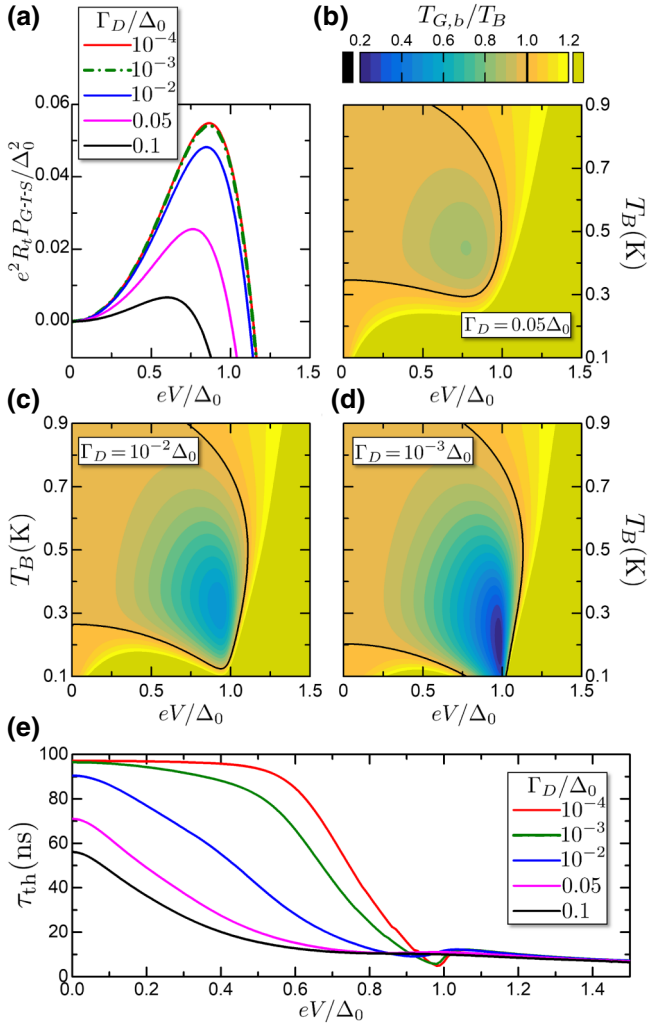

FIG. 8. (a) Cooling power at $T_G = T_B = 0.5$ K vs the bias V, for different values of Γ_D in the legend. (b)–(d) Contour plots of the ratio $T_{G,b}/T_B$ vs bias V and bath temperature T_B, for the values $\Gamma_D/\Delta_0 = 0.05, 10^{-2}, 10^{-3}$, respectively. (e) Response time $\tau_{\rm th}$ vs V at $T_B = 0.1$ K for the values of Γ_D in the legend, dirty *e*-ph coupling.

Effects on responsivity. The value of $\mathcal{R}$ is affected by Γ_D through the $T_{G,b}$ increase and, at the same time, by the reduction of $\partial I/\partial T$, since the smeared DOS peaks are translated in less sharp features of the $I(V)$ characteristics in temperature. Figure 9(a) shows $\mathcal{R}$ vs V for different values of Γ_D, for $T_B = 0.3$ K and clean e-ph coupling. The peak of $\mathcal{R}$ decreases by a factor 0.38 at $\Gamma_D = 10^{-2}$ and about 1 order of magnitude at $\Gamma_D = 0.05\Delta_0$.

Effects on NEP. The behavior of $\mathcal{R}$ on Γ_D is reflected in the NEP characteristics. Indeed, $\mathcal{R}$ is present in the denominators of the NEP components in Eqs. (37) and (43), while the numerators are weakly affected by Γ_D at $eV \simeq \Delta_0$. Figure 9(c) and (d) report the single junction $\mathcal{N}_{G\text{-}I\text{-}S}$ and the total NEP at $T_B = 0.3$ K, calculated in the same manner of Sec. V. Like the responsivity, the NEP worsen 1 order of magnitude to $\Gamma_D = 0.05\Delta_0$.

In summary, in this section, we show that the quality of the *G-I-S* junctions might play a role in the characteristics of the studied device. In particular, the Dynes parameter is detrimental for cooling and bolometric applications only when $\Gamma_D \gtrsim 10^{-2}\Delta_0$.

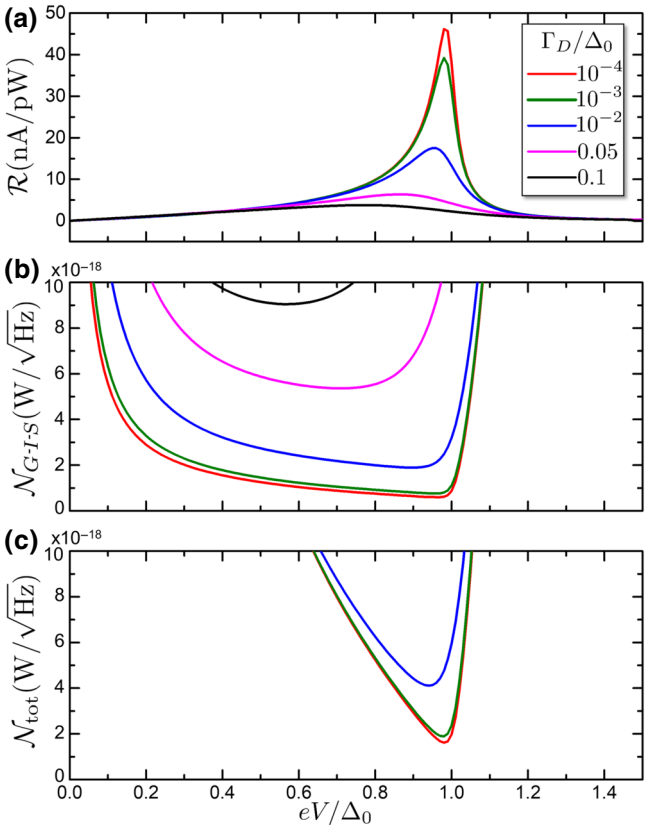

FIG. 9. Bolometric characteristics versus bias V for different values of the Dynes parameter Γ_D, in the legend. (a) Responsivity $\mathcal{R}$ at $T_B = 0.3$ K, clean e-ph coupling. (b) Junction NEP at $T_B = 0.3$ K. (c) Total NEP at $T_B = 0.3$ K, clean e-ph coupling. The NEP at $\Gamma_D/\Delta_0 = 5 \times 10^{-2}, 10^{-1}$ is out of scale, with respective minimum values $\simeq 1.1 \times 10^{-17}$ W/$\sqrt{\text{Hz}}$ and $\simeq 1.9 \times 10^{-17}$ W/$\sqrt{\text{Hz}}$.

VII. COMPARISON WITH OTHER BOLOMETRIC ARCHITECTURES

Bolometric technology is a very wide topic, stimulated mainly by challenges in astroparticle physics, e.g., study of the cosmic microwave background [108,109] or axion detection for dark-matter investigation [110–113]. The differences among bolometers concern many experimental features, such as fabrication issues, working temperature, readout schemes, figures of merit. Among all the different characteristics, detectors combining low noise with fast response speed are highly desirable. Nevertheless, in bolometer technology, there is a trade-off between NEP and response time. Indeed, a fast response time is associated with a fast heat dissipation through thermal channels. However, a large thermal dissipation corresponds to a low responsivity and to a large thermal coupling with external systems, both deteriorating the NEP. Hence, in an experimental setup, it is important to choose the right compromise between τ_{th} and the NEP $\mathcal{N}$ on the base of the specific requirements.

A comparison based on the various experimental features of all the different bolometric technologies is beyond the scope of this paper. Here, we compare our *S-I-G-I-S* with three bolometric architectures, similar in working principles or materials. The first architecture concerns *S-I-N-I-S* bolometers with built-in electron refrigeration [52–55,57,97,114]. Second, we consider *S-I-G-I-S* bolometers based on power-to-resistance conversion at $V = 0$ bias [14,74,98]. Finally, we consider also bolometers based on proximity effect in superconductor-normal-metal- superconductor (*S-N-S*) [115–117] and clean-contacted superconductor-graphene-superconductor (*S-G-S*) junctions [16,87].

S-I-N-I-S bolometers. Similarly to our device, *S-I-N-I-S* bolometers exploit the capability of a voltage bias to provide both cooling and extraction of the bolometric current signal. The theoretical work in Ref. [54] predicts $\tau \sim 0.2$ μs and $\mathcal{N} \sim 4 \times 10^{-18}$ W/$\sqrt{\text{Hz}}$ at temperature approximately 300 mK. Recent experiments have shown a response time $\tau \sim 2$ μs and $\mathcal{N} \sim 3 \times 10^{-18}$ W/$\sqrt{\text{Hz}}$ at this temperature, with a good accomplishment of the theoretical predictions. The response time of our device is faster than a *S-I-N-I-S* due to the very reduced heat capacity of graphene compared to metals. The NEP in our device and in the theoretical device of Ref. [54] are on the same order of magnitude, with a lower value in *S-I-G-I-S* due to the combined effect of a lower base temperature and lower heat dissipation. Another advantage of our device is the reduced heat leakage from the phonons, which is mirrored in low heat transport into the superconducting leads. This prevents the leads overheating, which is a problem present in *S-I-N-I-S* systems [43]. On the other hand, *S-I-N-I-S* systems take advantage of well-established fabrication techniques that guarantee high-quality junctions, while techniques for *G-I-S* junctions are still in development.

Zero-bias S-I-G-I-S bolometers. Another similar architecture consists of *S-I-G-I-S* devices biased at very low voltage [74,98]. In this case, the electronic refrigeration is absent, and bolometry is performed through the temperature-to-resistance transduction. Theoretically, these devices are predicted to have $\tau \sim 1\ \mu$s and $\mathcal{N} \sim 2 \times 10^{-19}\ \mathrm{W}/\sqrt{\mathrm{Hz}}$ at 100 mK [74]. In comparison with the theoretical device in Ref. [74], our device shows a NEP that is 1 order of magnitude larger but a faster response time. This is because the voltage bias increases the junction thermal conductance, thus increasing the noise contribution from the junctions but allowing a faster thermalization. Our device and the zero-bias *S-I-G-I-S* bolometers share the same fabrication issues concerning the quality of the tunnel junctions. At the state of the art, the measured NEP reached in zero-bias *S-I-G-I-S* is on the order of $10^{-17}\ \mathrm{W}/\sqrt{\mathrm{Hz}}$ [98].

S-N-S and S-G-S Josephson junction bolometers. Finally, we compare our system with another class of bolometers, based on clean-contacted *S-N-S* [115–117] or *S-G-S* [16] forming hybrid Josephson junctions. These systems exploit completely different physical phenomena and share with our *V*-biased *S-I-G-I-S* only the materials composing the detector. The transduction involves the temperature dependence of the junction kinetic inductance or the switching current. A recent paper reports a *S-N-S* bolometer that, at bath temperature 25 mK, shows a very low NEP $\mathcal{N} \sim 6 \times 10^{-20}\ \mathrm{W}/\sqrt{\mathrm{Hz}}$ and a quite long response time $\tau = 30\ \mu$s. Though, this response time is more than one order of magnitude faster in the class of low noise bolometers [117]. Compared to our device, the *S-N-S* ultimate experiment shows a longer response time but a better NEP.

A recent preprint [16] reports a very promising bolometer based on a *S-G-S* Josephson junction. The experiment is based on the measurement of the statistic distributions of the switching current (Fulton-Dunkleberger) versus the input power. Then, the NEP is estimated from the width of the distribution, since a larger standard deviation is associated with a larger uncertainty on the power signal measurement. In this way, the authors estimate a NEP $\mathcal{N} \sim 7 \times 10^{-19}\ \mathrm{W}/\sqrt{\mathrm{Hz}}$, reaching the fundamental limit imposed by the intrinsic thermal fluctuation of the bath temperature at 0.19 K [16]. The *S-G-S*-based architecture seems a promising path for further research in the field of low-noise bolometers.

VIII. CONCLUSIONS AND FURTHER DEVELOPMENTS

In this paper, we investigate electron cooling in graphene when tunnel contacted to form a *S-I-G-I-S* device and its application as a bolometer.

We study electron cooling by voltage biasing the junctions, exploiting the same mechanism of a *S-I-N-I-S* system. The low electron-phonon coupling in graphene allows having a sensible temperature decrease even for large-area graphene flakes and a high tunnel resistance ($100\ \mu\mathrm{m}^2$, 10 kΩ), differently from a *S-I-N-I-S* where a low tunnel resistance is required for adsorbing the larger phonon heating.

We then study the dynamics of the *S-I-G-I-S* cooler. We obtain the dependence of the thermal relaxation time on temperature and voltage bias and estimated its magnitude ($\tau_{\mathrm{th}} \sim 10$ ns).

Finally, we investigate the possibility of employing the cooled *S-I-G-I-S* system for bolometric applications. We find out that electron cooling enhances the responsivity and decreases the noise equivalent power. Moreover, the small electron-phonon coupling and the possibility of using high values of tunnel resistance allow reaching low noise equivalent power of the order $10^{-18}\ \mathrm{W}/\sqrt{\mathrm{Hz}}$. At the same time, the cooling mechanism increases the operation speed of the bolometer of more than 1 order of magnitude. Compared to the unbiased case, this makes the cooled *S-I-G-I-S* a suitable detector for THz communication [118–120] and cosmic microwave background [121,122] applications.

Further developments for our system could be explored. In particular, many known strategies already employed in *S-I-N-I-S* coolers and bolometers can be inherited. Among them, suspended graphene can show very interesting cooling characteristics due to the combined refrigeration of electrons and phonons, since in this case the latter are not connected to the substrate thermal bath [123–126].

ACKNOWLEDGMENTS

The authors acknowledge the European Research Council under the European Unions Seventh Frame-work Programme (FP7/2007-2013)/ERC Grant No. 615187—COMANCHE, the European Unions Horizon 2020 research and innovation programme under the Grant No. 777222 ATTRACT (Project T-CONVERSE), the Horizon research and innovation programme under Grant Agreement No. 800923 (SUPERTED), the Tuscany Region under the FARFAS 2014 project SCIADRO. M.C. acknowledges support from the Quant-EraNet project SuperTop. The work of F.P. work is partially supported by the Tuscany Government, POR FSE 2014–2020, through the INFN-RT2 172800 Project. A.B. acknowledges the CNR-CONICET cooperation program Energy conversion in quantum nanoscale hybrid devices and the Royal Society through the International Exchanges between the UK and Italy (Grant No. IES R3 170054). F.B. acknowledges the European Union's Horizon 2020 research and innovation program under Grant Agreement No. 696656—Graphene-Core1 and No. 75219 Graphene-Core2. S.R. acknowledges the support from the project PRA_2018_34 ("ANISE") from the University

of Pisa. S.R. and A.B. acknowledges the financial support from the project QUANTRA, funded by the Italian Ministry of Foreign Affairs and International Cooperation.

[1] O. A. Mukhanov, Energy-efficient single flux quantum technology, IEEE Trans. Appl. Supercond. **21**, 760 (2011).
[2] S. V. Polonsky, V. K. Semenov, P. I. Bunyk, A. F. Kirichenko, A. Y. Kidiyarov-Shevchenko, O. A. Mukhanov, P. N. Shevchenko, D. F. Schneider, D. Y. Zinoviev, and K. K. Likharev, New RFSQ circuits (Josephson junction digital devices), IEEE Trans. Appl. Supercond. **3**, 2566 (1993).
[3] M. H. Devoret and R. J. Schoelkopf, Superconducting circuits for quantum information: An outlook, Science **339**, 1169 (2013).
[4] A. Wallraff, D. I. Schuster, A. Blais, L. Frunzio, R.-S. Huang, J. Majer, S. Kumar, S. M. Girvin, and R. J. Schoelkopf, Strong coupling of a single photon to a superconducting qubit using circuit quantum electrodynamics, Nature **431**, 162 (2004).
[5] D. Vion, A. Aassime, A. Cottet, P. Joyez, H. Pothier, C. Urbina, D. Esteve, and M. H. Devoret, Manipulating the quantum state of an electrical circuit, Science **296**, 886 (2002).
[6] J. E. Mooij, T. P. Orlando, L. Levitov, L. Tian, C. H. van der Wal, and S. Lloyd, Josephson persistent-current qubit, Science **285**, 1036 (1999).
[7] A. Fornieri and F. Giazotto, Towards phase-coherent caloritronics in superconducting circuits, Nat. Nanotechnol. **12**, 944 (2017).
[8] F. Paolucci, G. Marchegiani, E. Strambini, and F. Giazotto, Phase-Tunable Thermal Logic: Computation with Heat, Phys. Rev. Appl. **10**, 024003 (2018).
[9] J. Clarke and A. I. Braginski, *The SQUID Handbook: Fundamentals and Technology of SQUIDs and SQUID Systems* (Wiley-VCH Verlag GmbH, 2005).
[10] J.-H. Storm, P. Hömmen, D. Drung, and R. Körber, An ultra-sensitive and wideband magnetometer based on a superconducting quantum interference device, Appl. Phys. Lett. **110**, 072603 (2017).
[11] F. Giazotto, J. T. Peltonen, M. Meschke, and J. P. Pekola, Superconducting quantum interference proximity transistor, Nat. Phys. **6**, 254 (2010).
[12] A. Ronzani, C. Altimiras, and F. Giazotto, Highly Sensitive Superconducting Quantum-Interference Proximity Transistor, Phys. Rev. Appl. **2**, 024005 (2014).
[13] F. H. L. Koppens, T. Mueller, P. Avouris, A. C. Ferrari, M. S. Vitiello, and M. Polini, Photodetectors based on graphene, other two-dimensional materials and hybrid systems, Nat. Nanotechnol. **9**, 780 (2014).
[14] X. Du, D. E. Prober, H. Vora, and C. B. Mckitterick, Graphene-based bolometers, Graphene 2D Mater. **1**, 1 (2014).
[15] H. Kraus, Superconductive bolometers and calorimeters, Supercond. Sci. Technol. **9**, 827 (1996).
[16] G.-H. Lee, D. K. Efetov, L. Ranzani, E. D. Walsh, T. A. Ohki, T. Taniguchi, K. Watanabe, P. Kim, D. Englund, and K. C. Fong, Graphene-based Josephson junction microwave bolometer, (2019), arXiv:1909.05413 [cond-mat.mes-hall].
[17] K. J. Tielrooij, L. Piatkowski, M. Massicotte, A. Woessner, Q. Ma, Y. Lee, K. S. Myhro, C. N. Lau, P. Jarillo-Herrero, N. F. van Hulst, and F. H. L. Koppens, Generation of photovoltage in graphene on a femtosecond timescale through efficient carrier heating, Nat. Nanotechnol. **10**, 437 (2015).
[18] K.-J. Tielrooij *et al.*, Out-of-plane heat transfer in van der Waals stacks through electron–hyperbolic phonon coupling, Nat. Nanotechnol. **13**, 41 (2017).
[19] A. El Fatimy, R. L. Myers-Ward, A. K. Boyd, K. M. Daniels, D. K. Gaskill, and P. Barbara, Epitaxial graphene quantum dots for high-performance terahertz bolometers, Nat. Nanotechnol. **11**, 335 (2016).
[20] C. Guarcello, A. Braggio, P. Solinas, G. P. Pepe, and F. Giazotto, Josephson-Threshold Calorimeter, Phys. Rev. Appl. **11**, 054074 (2019).
[21] P. Virtanen, A. Ronzani, and F. Giazotto, Josephson Photodetectors via Temperature-To-Phase Conversion, Phys. Rev. Appl. **9**, 054027 (2018).
[22] F. Giazotto, T. T. Heikkilä, G. P. Pepe, P. Helistö, A. Luukanen, and J. P. Pekola, Ultrasensitive proximity Josephson sensor with kinetic inductance readout, Appl. Phys. Lett. **92**, 162507 (2008).
[23] F. Giazotto, T. T. Heikkilä, A. Luukanen, A. M. Savin, and J. P. Pekola, Opportunities for mesoscopics in thermometry and refrigeration: Physics and applications, Rev. Mod. Phys. **78**, 217 (2006).
[24] J. T. Muhonen, M. Meschke, and J. P. Pekola, Micrometre-scale refrigerators, Rep. Prog. Phys. **75**, 046501 (2012).
[25] D. Sánchez, R. Sánchez, R. López, and B. Sothmann, Nonlinear chiral refrigerators, Phys. Rev. B **99**, 245304 (2019).
[26] F. Giazotto, F. Taddei, M. Governale, R. Fazio, and F. Beltram, Landau cooling in metal–semiconductor nanostructures, New J. Phys. **9**, 439 (2007).
[27] L. Vannucci, F. Ronetti, G. Dolcetto, M. Carrega, and M. Sassetti, Interference-induced thermoelectric switching and heat rectification in quantum Hall junctions, Phys. Rev. B **92**, 075446 (2015).
[28] F. Ronetti, M. Carrega, D. Ferraro, J. Rech, T. Jonckheere, T. Martin, and M. Sassetti, Polarized heat current generated by quantum pumping in two-dimensional topological insulators, Phys. Rev. B **95**, 115412 (2017).
[29] F. Dolcini and F. Giazotto, Adiabatic magnetization of superconductors as a high-performance cooling mechanism, Phys. Rev. B **80**, 024503 (2009).
[30] S. K. Manikandan, F. Giazotto, and A. N. Jordan, Superconducting Quantum Refrigerator: Breaking and Rejoining Cooper Pairs with Magnetic Field Cycles, Phys. Rev. Appl. **11**, 054034 (2019).
[31] P. G. Steeneken, K. Le Phan, M. J. Goossens, G. E. J. Koops, G. J. A. M. Brom, C. van der Avoort, and J. T. M. van Beek, Piezoresistive heat engine and refrigerator, Nat. Phys. **7**, 354 (2011).
[32] H. L. Edwards, Q. Niu, and A. L. de Lozanne, A quantum-dot refrigerator, Appl. Phys. Lett. **63**, 1815 (1993).

[33] H. L. Edwards, Q. Niu, G. A. Georgakis, and A. L. de Lozanne, Cryogenic cooling using tunneling structures with sharp energy features, Phys. Rev. B **52**, 5714 (1995).
[34] R. Hussein, M. Governale, S. Kohler, W. Belzig, F. Giazotto, and A. Braggio, Nonlocal thermoelectricity in a cooper-pair splitter, Phys. Rev. B **99**, 075429 (2019).
[35] J. Roßnagel, S. T. Dawkins, K. N. Tolazzi, O. Abah, E. Lutz, F. Schmidt-Kaler, and K. Singer, A single-atom heat engine, Science **352**, 325 (2016).
[36] B. Karimi and J. P. Pekola, Otto refrigerator based on a superconducting qubit: Classical and quantum performance, Phys. Rev. B **94**, 184503 (2016).
[37] F. Vischi, M. Carrega, P. Virtanen, E. Strambini, A. Braggio, and F. Giazotto, Thermodynamic cycles in Josephson junctions, Sci. Rep. **9**, 3238 (2019).
[38] P. Virtanen, F. Vischi, E. Strambini, M. Carrega, and F. Giazotto, Quasiparticle entropy in superconductor/normal metal/superconductor proximity junctions in the diffusive limit, Phys. Rev. B **96**, 245311 (2017).
[39] G. Marchegiani, P. Virtanen, F. Giazotto, and M. Campisi, Self-Oscillating Josephson Quantum Heat Engine, Phys. Rev. Appl. **6**, 054014 (2016).
[40] G. Marchegiani, P. Virtanen, and F. Giazotto, On-chip cooling by heating with superconducting tunnel junctions, EPL (Europhys. Lett.) **124**, 48005 (2018).
[41] M. Nahum, T. M. Eiles, and J. M. Martinis, Electronic microrefrigerator based on a normal-insulator-superconductor tunnel junction, Appl. Phys. Lett. **65**, 3123 (1994).
[42] M. M. Leivo, J. P. Pekola, and D. V. Averin, Efficient Peltier refrigeration by a pair of normal metal/insulator/superconductor junctions, Appl. Phys. Lett. **68**, 1996 (1996).
[43] H. Courtois, H. Q. Nguyen, C. B. Winkelmann, and J. P. Pekola, High-performance electronic cooling with superconducting tunnel junctions, C. R. Phys. **17**, 1139 (2016).
[44] H. Q. Nguyen, T. Aref, V. J. Kauppila, M. Meschke, C. B. Winkelmann, H. Courtois, and J. P. Pekola, Trapping hot quasi-particles in a high-power superconducting electronic cooler, New J. Phys. **15**, 085013 (2013).
[45] A. Hosseinkhani and G. Catelani, Proximity effect in normal-metal quasiparticle traps, Phys. Rev. B **97**, 054513 (2018).
[46] A. H. Castro Neto, F. Guinea, N. M. R. Peres, K. S. Novoselov, and A. K. Geim, The electronic properties of graphene, Rev. Mod. Phys. **81**, 109 (2009).
[47] S. Zihlmann, P. Makk, S. Castilla, J. Gramich, K. Thodkar, S. Caneva, R. Wang, S. Hofmann, and C. Schönenberger, Nonequilibrium properties of graphene probed by superconducting tunnel spectroscopy, Phys. Rev. B **99**, 075419 (2019).
[48] W. Chen and A. A. Clerk, Electron-phonon mediated heat flow in disordered graphene, Phys. Rev. B **86**, 125443 (2012).
[49] I. V. Borzenets, U. C. Coskun, H. T. Mebrahtu, Y. V. Bomze, A. I. Smirnov, and G. Finkelstein, Phonon Bottleneck in Graphene-Based Josephson Junctions at Millikelvin Temperatures, Phys. Rev. Lett. **111**, 027001 (2013).
[50] J. T. Karvonen and I. J. Maasilta, Influence of Phonon Dimensionality on Electron Energy Relaxation, Phys. Rev. Lett. **99**, 145503 (2007).
[51] J. T. Karvonen and I. J. Maasilta, Observation of phonon dimensionality effects on electron energy relaxation, J. Phys. Conf. Ser. **92**, 012043 (2007).
[52] M. Nahum and J. M. Martinis, Ultrasensitive-hot-electron microbolometer, Appl. Phys. Lett. **63**, 3075 (1993).
[53] M. Nahum, P. L. Richards, and C. A. Mears, Design analysis of a novel hot-electron microbolometer, IEEE Trans. Appl. Supercond. **3**, 2124 (1993).
[54] D. Golubev and L. Kuzmin, Nonequilibrium theory of a hot-electron bolometer with normal metal-insulator-superconductor tunnel junction, J. Appl. Phys. **89**, 6464 (2001).
[55] L. S. Kuzmin, I. A. Devyatov and D. Golubev, Cold-electron bolometer with electronic microrefrigeration and general noise analysis, Proc. SPIE **3465**, 193 (1998).
[56] D. R. Schmidt, K. W. Lehnert, A. M. Clark, W. D. Duncan, K. D. Irwin, N. Miller, and J. N. Ullom, A superconductor-insulator-normal metal bolometer with microwave readout suitable for large-format arrays, Appl. Phys. Lett. **86**, 053505 (2005).
[57] S. A. Lemzyakov, M. A. Tarasov, and V. S. Edelman, Investigation of the speed of a SINIS bolometer at a frequency of 350 GHz, J. Exp. Theor. Phys. **126**, 825 (2018).
[58] J. M. Dawlaty, S. Shivaraman, M. Chandrashekhar, F. Rana, and M. G. Spencer, Measurement of ultrafast carrier dynamics in epitaxial graphene, Appl. Phys. Lett. **92**, 042116 (2008).
[59] D. Brida, A. Tomadin, C. Manzoni, Y. J. Kim, A. Lombardo, S. Milana, R. R. Nair, K. S. Novoselov, A. C. Ferrari, G. Cerullo, and M. Polini, Ultrafast collinear scattering and carrier multiplication in graphene, Nat. Commun. **4**, 1987 (2013).
[60] F. Xia, T. Mueller, Y. Lin, A. Valdes-Garcia, and P. Avouris, Ultrafast graphene photodetector, Nat. Nanotechnol. **4**, 839 (2009).
[61] D. K. Efetov, R.-J. Shiue, Y. Gao, B. Skinner, E. D. Walsh, H. Choi, J. Zheng, C. Tan, G. Grosso, C. Peng, J. Hone, K. C. Fong, and D. Englund, Fast thermal relaxation in cavity-coupled graphene bolometers with a Johnson noise read-out, Nat. Nanotechnol. **13**, 797 (2018).
[62] T. Mueller, F. Xia, and P. Avouris, Graphene photodetectors for high-speed optical communications, Nat. Photonics **4**, 297 (2010).
[63] Z. Q. Li, E. A. Henriksen, Z. Jiang, Z. Hao, M. C. Martin, P. Kim, H. L. Stormer, and D. N. Basov, Dirac charge dynamics in graphene by infrared spectroscopy, Nat. Phys. **4**, 532 (2008).
[64] F. Wang, Y. Zhang, C. Tian, C. Girit, A. Zettl, M. Crommie, and Y. R. Shen, Gate-variable optical transitions in graphene, Science **320**, 206 (2008).
[65] B. Deng, Z. Liu, and H. Peng, Toward mass production of CVD graphene films, Adv. Mater. **31**, 1800996 (2019).

[66] L. Britnell, R. V. Gorbachev, R. Jalil, B. D. Belle, F. Schedin, M. I. Katsnelson, L. Eaves, S. V. Morozov, A. S. Mayorov, N. M. R. Peres, A. H. Castro Neto, J. Leist, A. K. Geim, L. A. Ponomarenko, and K. S. Novoselov, Electron tunneling through ultrathin boron nitride crystalline barriers, Nano Lett. **12**, 1707 (2012).

[67] J. Chen, C. Jang, S. Xiao, M. Ishigami, and M. S. Fuhrer, Intrinsic and extrinsic performance limits of graphene devices on SiO_2, Nat. Nanotechnol. **3**, 206 (2008).

[68] J. Martin, N. Akerman, G. Ulbricht, T. Lohmann, J. H. Smet, K. von Klitzing, and A. Yacoby, Observation of electron–hole puddles in graphene using a scanning single-electron transistor, Nat. Phys. **4**, 144 (2007).

[69] S. Das Sarma, S. Adam, E. H. Hwang, and E. Rossi, Electronic transport in two-dimensional graphene, Rev. Mod. Phys. **83**, 407 (2011).

[70] F. Amet, J. R. Williams, K. Watanabe, T. Taniguchi, and D. Goldhaber-Gordon, Selective Equilibration of Spin-Polarized Quantum Hall Edge States in Graphene, Phys. Rev. Lett. **112**, 196601 (2014).

[71] F. Amet, A. J. Bestwick, J. R. Williams, L. Balicas, K. Watanabe, T. Taniguchi, and D. Goldhaber-Gordon, Composite fermions and broken symmetries in graphene, Nat. Commun. **6**, 5838 (2015).

[72] A. S. Mayorov, D. C. Elias, I. S. Mukhin, S. V. Morozov, L. A. Ponomarenko, K. S. Novoselov, A. K. Geim, and R. V. Gorbachev, How close can one approach the Dirac point in graphene experimentally? Nat. Lett. **12**, 4629 (2012).

[73] L. Banszerus, M. Schmitz, S. Engels, J. Dauber, M. Oellers, F. Haupt, K. Watanabe, T. Taniguchi, B. Beschoten, and C. Stampfer, Ultrahigh-mobility graphene devices from chemical vapor deposition on reusable copper, Sci. Adv. **1**, e1500222 (2015).

[74] C. B. McKitterick, D. E. Prober, H. Vora, and X. Du, Ultrasensitive graphene far-infrared power detectors, J. Phys. Condens. Matter **27**, 164203 (2015).

[75] M. Maiti, K. Saha, and K. Sengupta, Graphene: Junctions and STM spectra, Int. J. Mod. Phys. B **26**, 1242002 (2012).

[76] H. Arjmandi-Tash, D. Kalita, Z. Han, R. Othmen, G. Nayak, C. Berne, J. Landers, K. Watanabe, T. Taniguchi, L. Marty, J. Coraux, N. Bendiab, and V. Bouchiat, Large scale graphene/h-BN heterostructures obtained by direct CVD growth of graphene using high-yield proximity-catalytic process, J. Phys.: Mater. **1**, 015003 (2018).

[77] D. V. Anghel and J. P. Pekola, Noise in refrigerating tunnel junctions and in microbolometers, J. Low Temp. Phys. **123**, 197 (2001).

[78] H.-O. Müller and K. A. Chao, Electron refrigeration in the tunneling approach, J. Appl. Phys. **82**, 453 (1997).

[79] T. Heikkilä, *The Physics of Nanoelectronics: Transport and Fluctuation Phenomena at Low Temperatures*, Oxford Master Series in Physics (OUP Oxford, 2013).

[80] A. A. Balandin, Thermal properties of graphene and nanostructured carbon materials, Nat. Mater. **10**, 569 (2011).

[81] Z. Chen, W. Jang, W. Bao, C. N. Lau, and C. Dames, Thermal contact resistance between graphene and silicon dioxide, Appl. Phys. Lett. **95**, 161910 (2009).

[82] H. Q. Nguyen, J. T. Peltonen, M. Meschke, and J. P. Pekola, Cascade Electronic Refrigerator Using Superconducting Tunnel Junctions, Phys. Rev. Appl. **6**, 054011 (2016).

[83] M. Camarasa-Gómez, A. Di Marco, F. W. J. Hekking, C. B. Winkelmann, H. Courtois, and F. Giazotto, Superconducting cascade electron refrigerator, Appl. Phys. Lett. **104**, 192601 (2014).

[84] D. K. Efetov and P. Kim, Controlling Electron-Phonon Interactions in Graphene at Ultrahigh Carrier Densities, Phys. Rev. Lett. **105**, 256805 (2010).

[85] E. H. Hwang and S. Das Sarma, Acoustic phonon scattering limited carrier mobility in two-dimensional extrinsic graphene, Phys. Rev. B **77**, 115449 (2008).

[86] R. S. Gonnelli, F. Paolucci, E. Piatti, K. Sharda, A. Sola, M. Tortello, J. R. Nair, C. Gerbaldi, M. Bruna, and S. Borini, Temperature dependence of electric transport in few-layer graphene under large charge doping induced by electrochemical gating, Sci. Rep. **5**, 9954 (2015).

[87] E. D. Walsh, D. K. Efetov, G.-H. Lee, M. Heuck, J. Crossno, T. A. Ohki, P. Kim, D. Englund, and K. C. Fong, Graphene-Based Josephson-Junction Single-Photon Detector, Phys. Rev. Appl. **8**, 024022 (2017).

[88] J. K. Viljas and T. T. Heikkilä, Electron-phonon heat transfer in monolayer and bilayer graphene, Phys. Rev. B **81**, 245404 (2010).

[89] F. Paolucci, G. Timossi, P. Solinas, and F. Giazotto, Coherent manipulation of thermal transport by tunable electron-photon and electron-phonon interaction, J. Appl. Phys. **121**, 244305 (2017).

[90] D. R. Schmidt, R. J. Schoelkopf, and A. N. Cleland, Photon-Mediated Thermal Relaxation of Electrons in Nanostructures, Phys. Rev. Lett. **93**, 045901 (2004).

[91] M. Meschke, W. Guichard, and J. P. Pekola, Single-mode heat conduction by photons, Nature **444**, 187 (2006).

[92] J. Jochum, C. Mears, S. Golwala, B. Sadoulet, J. P. Castle, M. F. Cunningham, O. B. Drury, M. Frank, S. E. Labov, F. P. Lipschultz, H. Netel, and B. Neuhauser, Modeling the power flow in normal conductor-insulator-superconductor junctions, J. Appl. Phys. **83**, 3217 (1998).

[93] L. A. Falkovsky, Thermodynamics of electron-hole liquids in graphene, JETP Lett. **98**, 161 (2013).

[94] F. Giazotto, F. Taddei, M. Governale, C. Castellana, R. Fazio, and F. Beltram, Cooling Electrons by Magnetic-Field Tuning of Andreev Reflection, Phys. Rev. Lett. **97**, 197001 (2006).

[95] P. J. Price, Hot electrons in a GaAs heterolayer at low temperature, J. Appl. Phys. **53**, 6863 (1982).

[96] Y. Ma, R. Fletcher, E. Zaremba, M. D'Iorio, C. T. Foxon, and J. J. Harris, Energy-loss rates of two-dimensional electrons at a $GaAs/Al_xGa_{1-x}As$ interface, Phys. Rev. B **43**, 9033 (1991).

[97] L. S. Kuzmin, A. L. Pankratov, A. V. Gordeeva, V. O. Zbrozhek, V. A. Shamporov, L. S. Revin, A. V. Blagodatkin, S. Masi, and P. de Bernardis, Photon-noise-limited cold-electron bolometer based on strong electron self-cooling for high-performance cosmology missions, Commun. Phys. **2**, 104 (2019).

[98] H. Vora, P. Kumaravadivel, B. Nielsen, and X. Du, Bolometric response in graphene based superconducting tunnel junctions, Appl. Phys. Lett. **100**, 153507 (2012).
[99] H. B. Heersche, P. Jarillo-Herrero, J. B. Oostinga, L. M. K. Vandersypen, and A. F. Morpurgo, Bipolar supercurrent in graphene, Nature **446**, 56 (2007).
[100] F. Giazotto and F. Taddei, Hybrid superconducting quantum magnetometer, Phys. Rev. B **84**, 214502 (2011).
[101] S. D'Ambrosio, M. Meissner, C. Blanc, A. Ronzani, and F. Giazotto, Normal metal tunnel junction-based superconducting quantum interference proximity transistor, Appl. Phys. Lett. **107**, 113110 (2015).
[102] P. L. Richards, Bolometers for infrared and millimeter waves, J. Appl. Phys. **76**, 1 (1994).
[103] F. Giazotto and J. P. Pekola, Josephson tunnel junction controlled by quasiparticle injection, J. Appl. Phys. **97**, 023908 (2005).
[104] R. C. Dynes, V. Narayanamurti, and J. P. Garno, Direct Measurement of Quasiparticle-Lifetime Broadening in a Strong-Coupled Superconductor, Phys. Rev. Lett. **41**, 1509 (1978).
[105] F. c. v. Herman and R. Hlubina, Microscopic interpretation of the Dynes formula for the tunneling density of states, Phys. Rev. B **94**, 144508 (2016).
[106] J. P. Pekola, V. F. Maisi, S. Kafanov, N. Chekurov, A. Kemppinen, Y. A. Pashkin, O.-P. Saira, M. Möttönen, and J. S. Tsai, Environment-Assisted Tunneling as an Origin of the Dynes Density of States, Phys. Rev. Lett. **105**, 026803 (2010).
[107] J. P. Pekola, T. T. Heikkilä, A. M. Savin, J. T. Flyktman, F. Giazotto, and F. W. J. Hekking, Limitations in Cooling Electrons Using Normal-Metal-Superconductor Tunnel Junctions, Phys. Rev. Lett. **92**, 056804 (2004).
[108] R. Crittenden, R. L. Davis, and P. J. Steinhardt, Polarization of the microwave background due to primordial gravitational waves, Astrophys. J. **417**, L13 (1993).
[109] U. Seljak and M. Zaldarriaga, Signature of Gravity Waves in the Polarization of the Microwave Background, Phys. Rev. Lett. **78**, 2054 (1997).
[110] L. Krauss, J. Moody, F. Wilczek, and D. E. Morris, Calculations for Cosmic Axion Detection, Phys. Rev. Lett. **55**, 1797 (1985).
[111] P. W. Graham, I. G. Irastorza, S. K. Lamoreaux, A. Lindner, and K. A. van Bibber, Experimental searches for the axion and axion-like particles, Annu. Rev. Nucl. Particle Sci. **65**, 485 (2015).
[112] Y. Hochberg, T. Lin, and K. M. Zurek, Detecting ultralight bosonic dark matter via absorption in superconductors, Phys. Rev. D **94**, 015019 (2016).
[113] CAST Collaboration, New CAST limit on the axion–photon interaction, Nat. Phys. **13**, 584 (2017).
[114] M. Nahum and J. M. Martinis, Hot-electron microcalorimeters as high-resolution x-ray detectors, Appl. Phys. Lett. **66**, 3203 (1995).
[115] J. Govenius, R. E. Lake, K. Y. Tan, V. Pietilä, J. K. Julin, I. J. Maasilta, P. Virtanen, and M. Möttönen, Microwave nanobolometer based on proximity Josephson junctions, Phys. Rev. B **90**, 064505 (2014).
[116] J. Govenius, R. E. Lake, K. Y. Tan, and M. Möttönen, Detection of Zeptojoule Microwave Pulses Using Electrothermal Feedback in Proximity-Induced Josephson Junctions, Phys. Rev. Lett. **117**, 030802 (2016).
[117] R. Kokkoniemi, J. Govenius, V. Vesterinen, R. E. Lake, A. M. Gunyhó, K. Y. Tan, S. Simbierowicz, L. Grönberg, J. Lehtinen, M. Prunnila, J. Hassel, A. Lamminen, O.-P. Saira, and M. Möttönen, Nanobolometer with ultralow noise equivalent power, Commun. Phys. **2**, 124 (2019).
[118] T. Kürner and S. Priebe, Towards THz communications – status in research, standardization and regulation, J. Infrared, Millimeter, Terahertz Waves **35**, 53 (2014).
[119] T. Nagatsuma, G. Ducournau, and C. C. Renaud, Advances in terahertz communications accelerated by photonics, Nat. Photonics **10**, 371 (2016).
[120] S. Ummethala, T. Harter, K. Koehnle, Z. Li, S. Muehlbrandt, Y. Kutuvantavida, J. Kemal, P. Marin-Palomo, J. Schaefer, A. Tessmann, S. K. Garlapati, A. Bacher, L. Hahn, M. Walther, T. Zwick, S. Randel, W. Freude, and C. Koos, THz-to-optical conversion in wireless communications using an ultra-broadband plasmonic modulator, Nat. Photonics **13**, 519 (2019).
[121] M. Tarasov, A. Sobolev, A. Gunbina, G. Yakopov, A. Chekushkin, R. Yusupov, S. Lemzyakov, V. Vdovin, and V. Edelman, Annular antenna array metamaterial with SINIS bolometers, J. Appl. Phys. **125**, 174501 (2019).
[122] K. Inomata and M. Kamionkowski, Circular polarization of the cosmic microwave background from vector and tensor perturbations, Phys. Rev. D **99**, 043501 (2019).
[123] P. J. Koppinen and I. J. Maasilta, Phonon Cooling of Nanomechanical Beams with Tunnel Junctions, Phys. Rev. Lett. **102**, 165502 (2009).
[124] P. J. Koppinen and I. J. Maasilta, Cooling of suspended nanostructures with tunnel junctions, J. Phys. Conf. Ser. **150**, 012025 (2009).
[125] P. J. Koppinen, T. J. Isotalo, and I. J. Maasilta, Boundary engineering for SINIS bolometers with integrated tunnel junction coolers, AIP Conf. Proc. 1185, 318 (2009).
[126] A. M. Clark, N. A. Miller, A. Williams, S. T. Ruggiero, G. C. Hilton, L. R. Vale, J. A. Beall, K. D. Irwin, and J. N. Ullom, Cooling of bulk material by electron-tunneling refrigerators, Appl. Phys. Lett. **86**, 173508 (2005).